Materials Today Sustainability 34 (2026) 101333

Contents lists available at ScienceDirect

Materials Today Sustainability

journal homepage: www.journals.elsevier.com/materials-today-sustainability

Biosynthesis of gold nanoparticles by a mining- adapted bacterial consortium: Physicochemical properties and environmental applications

Miranda Mpeta *, Job T. Tendenedzai, Shepherd M. Tichapondwa, Evans M.N. Chirwa

Water Utilization and Environmental Engineering Division, Department of Chemical Engineering, University of Pretoria, Pretoria, 0002, South Africa

ARTICLE INFO

Keywords:
Biosynthesized nanoparticles
Catalytic properties
Antimicrobial activity

ABSTRACT

Biological synthesis of gold nanoparticles (AuNPs) offers an eco-friendly alternative to conventional synthesis methods. A bacterial consortium (comprising *Klebsiella pneumoniae*, *Stenotrophomonas maltophilia*, *Acinetobacter bereziniae*, and *Bacillus cereus)* was used for AuNPs biosynthesis. Physicochemical characteristics and functional properties of AuNPs were evaluated. Techniques including UV-Vis spectroscopy, Transmission Electron Microscopy (TEM), Fourier Transform Infrared (FTIR) spectroscopy, Dynamic light scattering (DLS), and X-ray diffraction (XRD) were used to characterize the AuNPs. Results showed that particle size distribution, surface charge, and crystallinity were influenced by biomolecular capping. When applied in antimicrobial activity against *Enterococcus* spp. and *Klebsiella pneumoniae* inhibition was significant at 25 μg/mL and most pronounced at 50 μg/mL. TEM analysis confirmed cell membrane rupture as the primary antimicrobial mechanism. AuNPs were incorporated into TiO_2 (Degussa P25) to form a composite (TiO_2/0.5 wt% AuNP). Scanning electron microscopy (SEM, UV-Visible Diffuse Reflectance Spectroscopy (UV–Vis DRS) and Brunauer-Emmett-Teller (BET) analysis were employed to characterize the composite. The composite showed enhanced surface reactivity and reduced band gap (from 3.1 to 2.7 eV) when compared with pristine TiO_2. The composite exhibited enhanced Rhodamine B degradation under both visible light and sunlight. First-order photocatalytic kinetics was confirmed with high correlation coefficients ($R^2 \geq 0.92$), validating the model. Enhanced reaction rates for the composite were noticed under visible light, the rate constant increased by 1.67-fold (0.0025 vs. 0.0015 min^{-1}), and under sunlight ($R^2 \geq 0.96$), by 2.5-fold (0.019 vs. 0.0075 min^{-1}). Results highlight the importance of biosynthesized nanomaterials and their role in targeted applications in catalysis and environmental remediation.

1. Introduction

Gold nanoparticles have gained significant attention due to their unique physicochemical properties. High surface-to-volume ratio, high biocompatibility and local surface plasmon resonance (LSPR) give them their functional advantage [1–3]. Due to these unique properties, AuNPs have been useful for applications in environmental remediation, catalysis, biosensing and drug delivery [2,4,5]. In environmental remediation, their outstanding catalytic properties make them capable of reducing persistent organic pollutants and other environmental contaminants [6]. In water and soil environments, functionalized AuNPs can effectively remove toxic substances through several mechanisms. AuNPs can reduce environmentally toxic hexavalent chromium, Cr (VI) to less toxic trivalent chromium, Cr (III) [7]. Their high surface area and unique surface chemistry allow for the adsorption and breakdown of organic pollutants. Abubakar [8] highlighted that AuNPs can break down compounds including pesticides and industrial chemicals. Their use in environmental applications extends to sensing and detection technologies. Parameswari [9] confirmed the ability of gold nanoparticle-based sensors to detect trace amounts of environmental contaminants. In identification of potential ecological threats, AuNPs allow early detection due to their high sensitivity and specificity [10,11]. When analyzing environmental samples, AuNPs allow for colorimetric detection methods that can quickly identify pollutants due to their exceptional surface plasmon resonance [9,12].

Chemical and physical methods are conventionally used to synthesize AuNPs. Some of the methods often involve toxic reagents and are energy intensive posing environmental and health risks [13]. The use of microorganisms in biosynthesis of nanoparticles has emerged as a promising alternative. This green route for nanomaterial production has

* Corresponding author.
E-mail addresses: u24054276@tuks.co.za (M. Mpeta), job.tendenedzai@tuks.co.za (J.T. Tendenedzai), shepherd.tichapondwa@up.ac.za (S.M. Tichapondwa), evans.chirwa@up.ac.za (E.M.N. Chirwa).

https://doi.org/10.1016/j.mtsust.2026.101333
Received 24 October 2025; Received in revised form 16 January 2026; Accepted 15 February 2026
Available online 16 February 2026

been confirmed especially for low concentration ores or tailings [4,14,15]. Compared to other biological systems, bacteria are specifically preferred. Their fast growth rates, ease of genetic manipulation, and ability to mediate metal reduction through various enzymatic and non-enzymatic pathways, make them attractive [4,16]. Bacteria act as both reducing and stabilizing agents during this biosynthesis process. Paesa [17] confirmed that nanoparticle size, morphology, and surface chemistry of biogenic AuNPs are influenced by biomolecules secreted by bacteria.

The influence of bacterial strain diversity and consortia combinations on the physicochemical properties of the resulting nanoparticles remains underexplored. Despite the reports on bacterial synthesis of AuNPs by Malarkodi [16] and Thirumurugan [18] different bacterial taxa produce distinct extracellular metabolites and possess varying enzymatic capabilities. All these factors significantly impact the nucleation and growth dynamics of AuNPs. While previous studies have demonstrated enhanced photocatalytic activity of AuNPs, they often lack systematic characterization of SPR-mediated charge transfer mechanisms. There is also a gap in establishing clear synthesis–-structure–property relationships. In addition, antimicrobial applications against priority drug-resistant pathogens remain largely unexplored. To address these gaps, the present study was guided by the following hypotheses: (i) consortium-derived AuNPs exhibit distinct physicochemical properties that can be systematically characterized and correlated with antimicrobial efficacy, (ii) these nanoparticles differentially affect Gram-negative and Gram-positive bacteria, including multidrug-resistant *Klebsiella pneumoniae* and *Enterococcus* spp., (iii) incorporation of consortium-derived AuNPs modifies TiO_2 properties in ways that enhance SPR-mediated charge transfer, and (iv) such modifications improve photocatalytic performance under both UV and visible light.

For the biosynthesis of AuNPs, a bacterial consortium comprising *Klebsiella pneumoniae, Stenotrophomonas maltophilia, Acinetobacter bereziniae*, and *Bacillus cereus* was employed, as synergistic interactions among these strains collectively enhance biosynthesis efficiency and nanoparticle stability compared to individual strains [19]. The manuscript first details the consortium-mediated biosynthesis process and comprehensive characterization of the resulting AuNPs using spectroscopic, microscopic, and diffraction techniques. The antimicrobial activity of the biogenic AuNPs is then evaluated against representative bacterial strains, with mechanistic insights provided through electron microscopy. Finally, the incorporation of AuNPs into a TiO_2 matrix is presented, followed by structural and optical characterization of the composite and assessment of its photocatalytic performance for organic dye degradation under visible light and sunlight conditions. By establishing explicit correlations between nanoparticle properties and their functional outcomes, this study advances targeted synthesis strategies for sustainable nanotechnology, with direct relevance to environmental remediation (SDG 6) and responsible production (SDG 12).

2. Materials and methods

2.1. Bacterial strains and culture conditions

Four bacterial strains were employed for the biosynthesis of AuNPs: *Klebsiella pneumoniae, Stenotrophomonas maltophilia, Acinetobacter bereziniae* and *Bacillus cereus* (as identified using 16S rRNA sequencing). These strains had been previously isolated from gold mine tailings and mine wastewater samples, representing naturally adapted populations from metal-rich environments. More details on the isolation and culturing of bacteria are in the previous study by Mpeta et al. [19]To culture Au (III)-tolerant bacteria, 0.5 g of each sample (stored at 4 °C) was inoculated into 150 mL of sterile Tryptone Soy Broth (TSB) supplemented with 2 mL of 10 ppm Au (III) (as chloroauric acid). Cultures were incubated at 35 ± 2 °C with shaking at 120 rpm for 24 h (Labex Model 353). After enrichment, isolates were streaked onto Au (III)-amended agar plates and incubated overnight at 35 °C under static conditions. For liquid cultures, single colonies were inoculated into 100 mL TSB and grown at 35 ± 2 °C, 120 rpm for 24 h to reach stationary phase. Equal volumes (10 mL) of each strain were then pooled aseptically into 100 mL of TSB (pH 7.0) to form the bacterial consortium, which was incubated under the same conditions for 24 h prior to nanoparticle biosynthesis.

2.2. Preparation of gold precursor solution

Chloroauric acid ($HAuCl_4 \cdot 3H_2O$, ≥99.9% purity; Sigma-Aldrich, USA) was employed as the gold precursor. A 1 mM aqueous stock solution was prepared in deionized water and sterilized through a 0.22 μm membrane filter prior to use. The concentration of Au (III) ions in the stock was confirmed by atomic absorption spectroscopy (AAS; PerkinElmer AAnalyst 400, USA) at 242.8 nm using a 290 mA gold hollow cathode lamp. To prevent photodegradation, the solution was stored in amber plastic bottles at 4 °C until required.

2.3. Biosynthesis of gold nanoparticles

For nanoparticle biosynthesis, 10 mL of actively growing bacterial culture was added to 90 mL of reaction medium containing the gold precursor ($HAuCl_4$). Three media types were tested: (i) $HAuCl_4$ solution in deionized water, (ii) Tryptone Soy Broth (TSB), and (iii) mineral salt medium (MSM), to evaluate the influence of medium composition on AuNP yield. Reactors were placed in an incubator with shaker at 35 ± 2 °C under dark conditions for 24 h. Nanoparticle formation was initially monitored by the characteristic color change [20] and confirmed by checking the peaks using UV–Vis spectroscopy as explained in section 2.4. Controls for the reaction included: (i) $HAuCl_4$ without bacterial culture and (ii) bacterial culture without $HAuCl_4$. Detailed optimization of culture media composition and quantitative yield analysis are subjects of ongoing investigation and will be reported separately.

2.4. Characterization of AuNPs

AuNP formation and optical properties were confirmed using UV-Vis spectrophotometry (PerkinElmer Lambda 950 model) over a range of 300–800 nm, with surface plasmon resonance peaks between 520 and 575 nm showing successful nanoparticle synthesis [20,21]. The transmission electron microscopy (TEM), Jeol 2100 FEGTEM model was used to analyze the morphology of AuNPs. Standard sample preparation protocols were followed were prepared through as outlined by Tendenedzai [22]. These involved glutaraldehyde fixation, osmium tetroxide post-fixation, resin embedding, and ultrathin sectioning.

Particle size distribution, surface charge, and stability of colloids were measured via dynamic light scattering and zeta potential measurements using Malvern Zetasizer Nano ZS (Ver. 7.11). Functional groups responsible for nanoparticle stabilization were identified through FTIR spectroscopy (Shimadzu IRSpirit X-QATR-S, 4000–400 $cm^{-1}$of dried AuNP samples. Crystallographic structure was confirmed by X-ray diffraction (Rigaku PANalytical X'Pert Pro, Cu Kα radiation, 2θ = 20–80°), revealing characteristic peaks.

2.5. Synthesis of TiO_2/AuNPs composite

To prepare TiO_2- AuNPs composites, bacterially synthesized gold nanoparticles (AuNPs) were first centrifuged at 9000 rpm for 15 min, washed three times with distilled water to remove bacterial metabolites, and resuspended in 50 mL distilled water, with concentration confirmed via UV-Vis spectroscopy. Concurrently, 5 g of TiO_2 powder (Degussa P25, a commercial mixed-phase TiO_2 photocatalyst consisting of ~80% anatase and ~20% rutile) acquired from Sigma Aldrich Merck (Germany) was used. It was first cleaned with distilled water, activated in

100 mL of 0.1 M HCl for 30 min, washed until neutral (pH 6-7), and dried at 80 °C for 2 h. The activated TiO_2 (2 g) was then suspended in 100 mL distilled water, sonicated for 30 min, and adjusted to pH 4-5 with 0.1 M HCl for optimal AuNP attachment [23]. The AuNP suspension was slowly mixed with the TiO_2 suspension, stirred gently for 15 min, maintained at pH 4-5, and stirred for 4 h with heating to 60 °C for enhanced attachment. After allowing it to settle for 30 min, the TiO_2/AuNPs suspension was centrifuged at 9000 rpm for 10 min. The resultant pellet was washed four times with deionized water followed with ethanol (once). The pellet was dried at 75 °C overnight in a vacuum oven [24]. To remove organic residues, the dried composite was then calcined in a furnace at 300 °C for 2 h. The composite was allowed to cool and then ground into a uniform powder using mortar and pestle. The final product was put in a closed container and stored in dark, dry place.

2.6. Characterization of TiO_2/AuNPs

Multiple analytical techniques were used to characterize the composite of TiO_2 doped with AuNPs (TiO_2/AuNP). XRD was employed to analyze crystalline phases and structural integrity of the composite. The model used was equipped with PANalytical X'Pert Pro diffractometer with an X'Celerator detector and variable divergence. FTIR spectroscopy was used to identify the surface functional groups responsible for composite stabilization. SEM (model FEGSEM Zeiss 540 Ultra) was used to examine particle size and morphology. UV-Visible Diffuse Reflectance Spectroscopy (UV–Vis DRS) model HITACHI U-3900 enabled bandgap determination through Tauc plot analysis for photocatalytic assessment. Brunauer-Emmett-Teller (BET) analysis (Micromeritics TriStar II, Model 3020, U.S.A) measured specific surface area and porosity characteristics critical for photocatalytic performance. All these analyses were done on both pure TiO_2 (Degussa P25) and the TiO_2 doped with AuNPs.

2.7. Functional assays

2.7.1. Antimicrobial activity assay

The antimicrobial activity of the biosynthesized AuNPs was assessed against *Enterococcus* spp. and *Klebsiella pneumoniae* using the agar well diffusion method. Cultures were incubated for 24 h at 37 °C, after which the inhibition zone diameters were measured. Additionally, growth of *Enterococcus* spp and *Klebsiella pneumoniae* in broth with varying concentrations of (0-50 μg/mL) of AuNPs at 37 °C was measured (as OD_{600}) over a 40-h period using the UV-Vis. *Enterococcus* was selected as the test organism because it is both an indicator of faecal contamination in water and a clinically relevant pathogen.*Klebsiella pneumoniae* was selected as it is a multidrug resistant (MDR) pathogens, hence clinically relevant. Previous studies have commonly used *Escherichia coli* and *Vibrio cholerae* as model organisms [21,25]; however, this study focused on *Enterococcus* to broaden understanding of AuNP antimicrobial effects.

2.7.2. Catalytic degradation of rhodamine B dye

A 10 ppm stock solution of Rhodamine B was prepared in deionized water and used in all photocatalytic experiments. For each test, 0.1 g of AuNP-doped TiO_2 catalyst was suspended in 100 mL of the dye solution. The suspension was kept in the dark for 30 min to establish adsorption–desorption equilibrium before irradiation. Photocatalytic degradation was then carried out under two conditions: visible light provided by fluorescent lamp (216 Watts) and natural sunlight with solar irradiation between 346 and 629 Watts/m^2. Aliquots were withdrawn at regular intervals during the reaction, and dye degradation was monitored spectrophotometrically. Degradation and adsorption rate were calculated as shown in equations (1) and (2):

$$\%\, C_{ads} = \frac{C_{initial} - C_0}{C_{initial}} \times 100\% \qquad \text{Equation 1}$$

$$\%\, C_{deg} = \frac{C_0 - C_t}{C_0} \times 100\% \qquad \text{Equation 2}$$

where: $C_{initial}$ is concentration of dye at the start of dark phase.
C_0 is concentration of dye at the onset of light exposure.
C_t is concentration of dye at the end of t hours, $0 \leq t \leq 4$.

3. Results and discussions

3.1. Characterization of biosynthesized AuNPs

The diverse metabolic capabilities of *K. pneumoniae, S. maltophilia, A. bereziniae*, and *B. cereus* are maximized in nutrient-rich, neutral conditions, producing optimal AuNPs [19]. The biosynthesized AuNPs were characterized by methods outlined in this section.

3.1.1. Visual and UV VIS confirmation of AuNP synthesis

The experiments investigated how bacterial growth media influenced the biosynthesis of gold nanoparticles. As described in the methodology, the bacterial consortium was incubated in three distinct media: deionized water, TSB broth, and MSM, each supplemented with $HAuCl_4$ (1 mM). After 24 h of incubation with the gold precursor, all reactors containing the consortium exhibited distinct color changes which were influenced by the specific medium in which they were cultivated.

UV-Vis spectroscopy (Fig. 1a) confirmed the successful synthesis of gold nanoparticles (AuNPs) by the bacterial consortium in various media, with distinct surface plasmon resonance (SPR) peaks indicating nanoparticle formation and size. In deionized water, a sharp SPR peak at 515 nm suggested the presence of small AuNPs (5–10 nm). In mineral salt medium (MSM, pH 7), a prominent SPR peak at 525 nm with an absorbance of 1.3 a.u. The observed SPR peak for AuNPs synthesized under controlled metabolic conditions appeared between 15 and 30 nm. Shah [26] also confirmed this link between size ranges to regulated microbial activity. There was a higher absorbance peak of 1.5 a.u at 575 nm (Fig. 1a) for AuNPs produced in nutrient broth. Duman and Akda [21] confirmed a single SPR peak at 527 nm in similar systems. There were smaller nanoparticles (5- 10 nm) peaking between 515 and 520 nm. The medium-sized range (20- 60 nm) was peaking between 524 and 540 nm while larger ones (80-100 nm) between 553 and 572 nm (Fig. 1a and c). In support, Shah et al., (2014) identified the correlation between nanoparticle size and SPR wavelength. Control samples of uninoculated MSM with 1 mM $HAuCl_4$ and consortium supernatant without $HAuCl_4$, displayed no absorbance in the 500- 600 nm range. This confirmed the specificity of the SPR peaks to AuNP formation.

The visual observations illustrated in Fig. 1b and d are consistent with these results. In protein-rich TSB, the resultant AuNPs showed a deep blue-purple color. This suggested larger or aggregated particles (above 50 nm) stabilized by protein capping mechanisms as described by Khan and Ahmad [27]. AuNPs produced in MSM were wine-red in color, that is mineral rich also containing glucose as a carbon source. These were indicative of medium-sized particles. Ruby red color was noted for AuNPs synthesized in deionized water. These were suggestive of smaller particle sizes. Media supplemented with specific carbohydrate sources, such as glucose in MSM, influence the capping protein profile, leading to distinct surface functionalities of resulting AuNPs [28,29].

While different media were tested, mineral salt medium (MSM) emerged as the most suitable medium for subsequent experiments. This was due to an optimal environment it offers for producing smaller and more uniform AuNPs compared to TSB. MSM also yielded a higher nanoparticle yield than deionized water due to its balanced nutrient composition. The medium's neutral pH (7) played a critical role in supporting bacterial growth[19]. Additionally, it enhanced enzyme activity while promoting biomolecule deprotonation. Both factors enhanced the reduction and capping processes during formation of

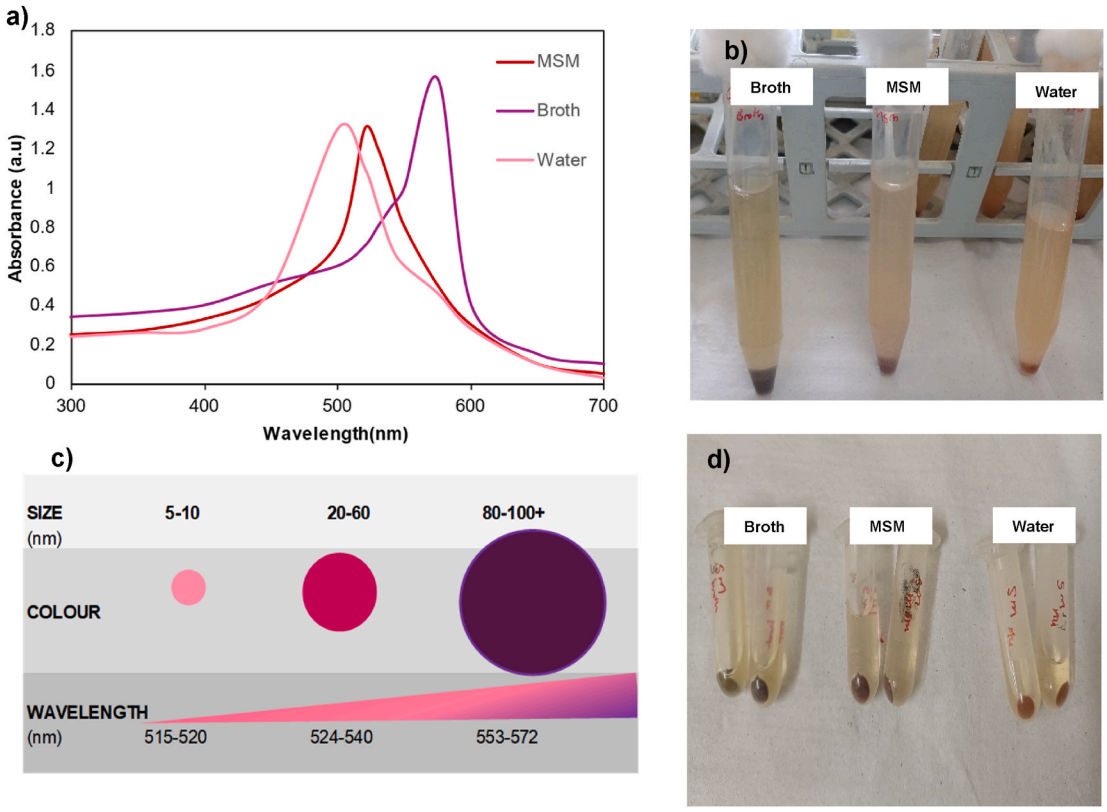

Fig. 1. a) UV- VIS absorption spectrum of gold nanoparticles (AuNPs) in aqueous mineral salt media (MSM), broth and water reduced by consortium b) Samples from reactor after 24h of Au (III) bioreduction in different media broth, MSM and deionized water c) Nanoparticle size ranges and corresponding color and wavelength d) Samples after centrifuging.

AuNPs [28,29]. This observation is consistent with previous findings that neutral pH is favorable for the growth and metabolic activity of the bacterial consortium used in this study [19]. In contrast, acidic conditions tend to stress bacterial cells and promote protonation of functional groups on capping agents, leading to reduced nanoparticle stability. Alkaline conditions negatively affect nanoparticle morphology and size as they cause conformational changes in biomolecules [21].

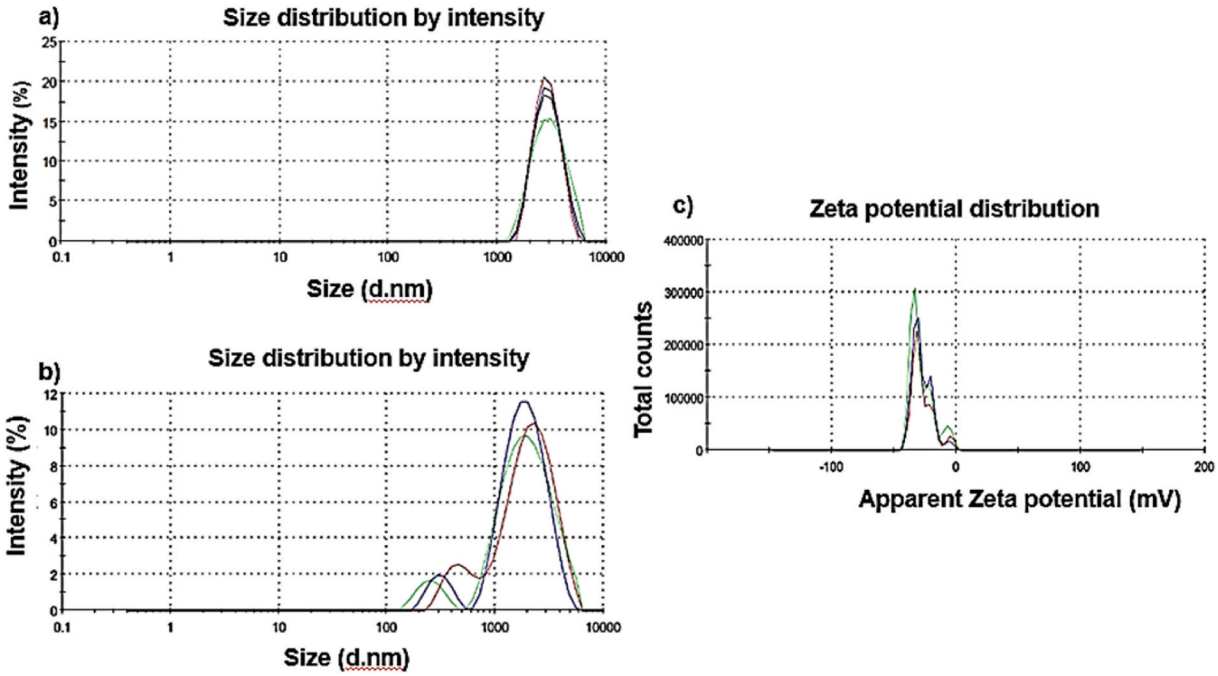

Fig. 2. a) Size distribution curve after 10mins of sonication. b) Size distribution after 15mins of sonication. c) Zeta potential for biosynthesized AuNPs in MSM at pH7.

3.1.2. Particle size distribution and stability

The particle-size distribution peak deconvolution was performed using the software package Origin 2021b (Origin lab Corporation, Northampton, MA, USA).

Size distribution analysis of biosynthesized AuNPs under different sonication conditions was determined by dynamic light scattering (DLS) using a zeta sizer (Fig. 2a). After 10 min of sonication as shown in Fig. 2a, the size distribution was dominated by micro-scale particles indicating agglomeration. However, a distinct peak corresponding to nanoscale particles emerged when sonication was extended by an additional 5 min (Fig. 2b). This supported prolonged sonication partially disrupted agglomeration confirming the presence of nanoparticles. The observed change in the size distribution highlights the effectiveness of prolonged sonication in reducing particle aggregation, though complete dispersion into individual nanoparticles was not achieved under these conditions. Increased sonication time or higher sonication intensity could enhance dispersion[30]. This could result in narrower size distribution and reflect the true nanoscale characteristics more accurately [30].

To determine colloidal stability, zeta potential analysis of the biosynthesized AuNPs yielded a value of −29.9 mV (Fig. 2c). This value was associated with good colloidal stability as it exceeded the critical threshold of ±15 mV. However, the presence of larger particle sizes, as confirmed by TEM analysis (discussed in subsequent sections), suggests that some agglomeration persists, possibly due to high surface charge interactions [25].

3.1.3. Morphological characterization and size distribution

The sphericities of the nanoparticles were estimated by image analysis of the TEM figures using the Software Package ImageJ (National Institutes of Health, Bethesda, MD, USA). From the TEM analysis, individual nanoparticles were spherical in shape and between 20 and 60 nm as shown in Fig. 3a-c, and some that were hexagonal in shape as shown in Fig. 3d-f. The spherical AuNPs were found in both inside and outside of cell environments. The spherical AuNPs showed agglomeration possibly due to high surface charge, and the large particles tend to remain extracellular. Hexagonal AuNPs and flakes, averaging 125 nm, were predominantly found outside cells. The formation of different shapes is attributed to catalytic reduction processes occurring on specific Miller planes of seed surfaces, where growth patterns depend on the exposed crystallographic faces [31].

Hydrodynamic diameter measurements obtained via Zetasizer analysis reflected the solvated and aggregated states of the synthesized AuNPs, whereas transmission electron microscopy (TEM) revealed the core sizes of individual particles. TEM imaging (Fig. 3) indicated that the core sizes of AuNPs were smaller than the hydrodynamic range reported by the Zetasizer (100-1000 nm). The smallest particles measured approximately 20 nm comprising 5% of the sample while the largest reached 125 nm accounting for 1.3% of the sample. Based on the TEM-derived size distribution (Fig. 4), the mean particle size was 52.49 nm. The highest frequency of 23% constituted of the AuNPs in the 60-70 nm range. Large particles in the form of agglomerates were observed both intracellularly and extracellularly. These agglomerates, formed from individual particles, contributed to the broader size variation observed outside bacterial cells [6,32]. The skewed distribution profile recorded by the Zetasizer was due to these agglomerates. These large hydrodynamic sizes were likely influenced by interparticle interactions and solvation effects [30,33].

Discrepancies in biosynthesized gold nanoparticle (AuNP) sizes between dynamic light scattering (DLS Zetasizer) and transmission electron microscopy (TEM) arise from methodological differences, amplified by biological coatings and polydispersity biases. DLS measures hydrodynamic diameters in solution, including the AuNP core plus biomolecular stabilizers such as proteins, polysaccharides (from microbial synthesis), resulting in larger sizes due to solvation and capping layers [27–29,34]. TEM, however, images the dried metallic core, excluding

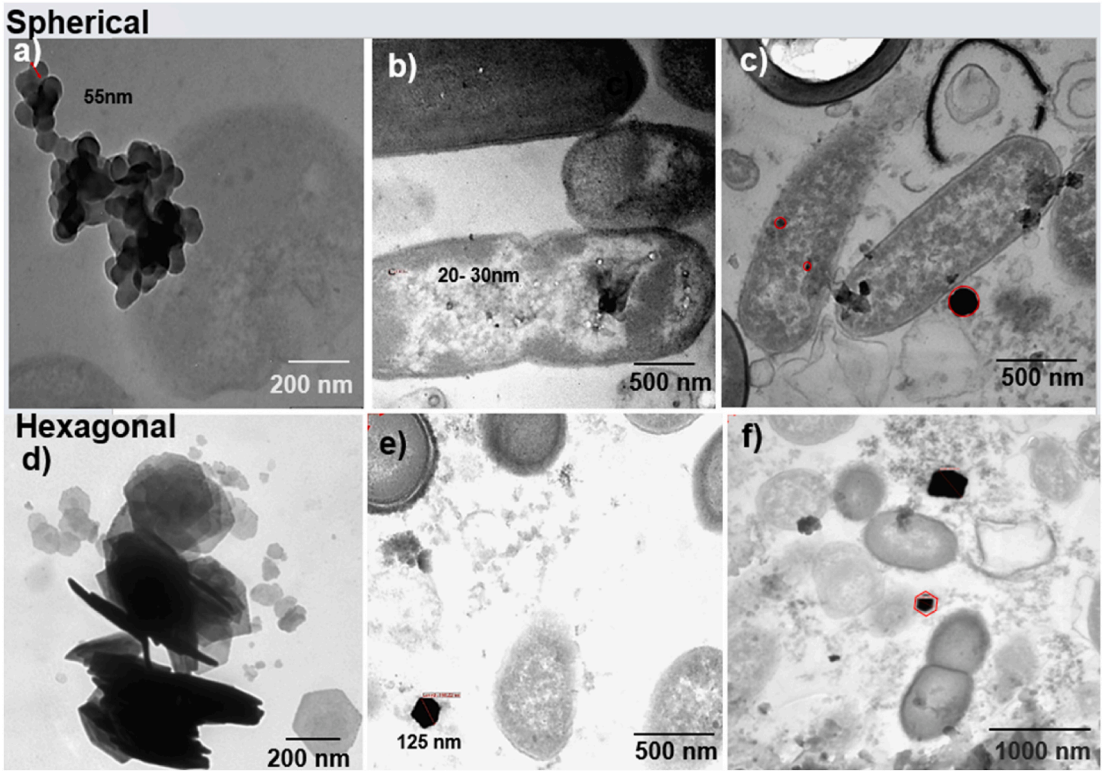

Fig. 3. TEM images showing different sizes and shapes of AuNPs a) 55 nm average size spherical AuNPs agglomerated b) Spherical AuNPs below 50 nm inside the bacterial cell c) Both extra and intracellular spherical AuNPs d) Hexagonal AuNPs and flakes outside the cells 200 nm average size e) and f) extracellular hexagonal between 100 and 200 nm.

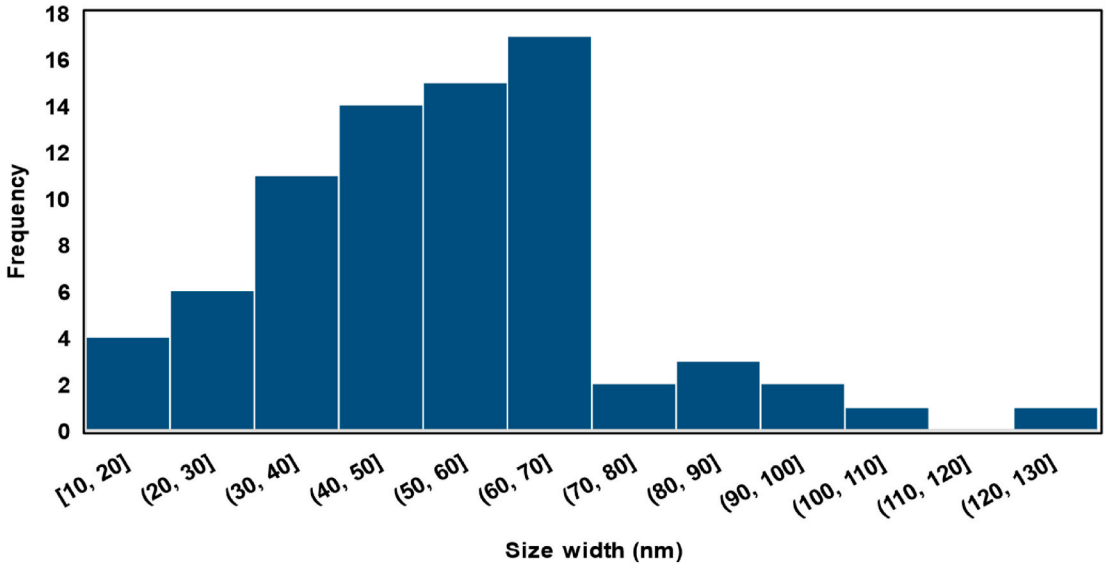

Fig. 4. Particle size distribution using TEM analysis after bioreduction of 1 mM $HAuCl_4$.

these shells and yielding smaller primary sizes [33]. In AuNPs made by a bacterial consortium, extracellular biomolecules form thick layers that can be detected by Dynamic Light Scattering (DLS) but are not visible in the core view of Transmission Electron Microscopy (TEM). The variation in particle sizes (polydispersity) can make DLS measurements less reliable because the scattered light intensity increases with the sixth power of the particle radius. This means larger particles or clumps heavily influence the results and make the average size appear larger in mixed samples [33]. It should be noted that DLS measurements are intensity-weighted and therefore disproportionately influenced by larger particles or minor aggregates present in suspension. As a result, DLS provides a less reliable estimate of primary particle size for heterogeneous biogenic AuNPs and is more appropriately interpreted as a measure of hydrodynamic behavior and colloidal stability rather than true core dimensions. In contrast, TEM provides a more accurate size distribution by counting individual particles directly. Thus, both techniques are complementary for fully characterizing biosynthesized AuNPs.

3.1.4. *Surface chemistry via FTIR*

To investigate the functional groups, present in biosynthesized gold nanoparticles using the bacterial consortium, Fourier transform infrared spectroscopy (FTIR) was used. The FTIR spectrum of the synthesized nanoparticles and associated biomolecules is shown in Fig. 5. The FTIR spectroscopy revealed key functional groups associated with the biosynthesized gold nanoparticles. A broad peak around 3300 cm^{-1} was attributed to O-H stretching vibrations of hydroxyl groups, from alcohols or phenols [20]. A weaker peak at 2922 cm^{-1} corresponded to C-H stretching vibrations, from methylene (-CH_2-) or methyl (-CH_3) groups in lipids, proteins, or polysaccharides [20,35]. These biomolecules, including lipopeptides from *Bacillus* species, exopolysaccharides from *Klebsiella pneumoniae* (a major contributor in this consortium), and extracellular polymeric substances (EPS) from *Stenotrophomonas maltophilia*, likely stabilize AuNPs through hydrophobic interactions. The presence of a peak at ~1679 cm^{-1}, associated with C=O stretching of carbonyl groups, and an amide I band between 1630 and 1650 cm^{-1} suggest the coexistence of proteins[36], potentially via amino acid residues containing -COO^- groups. The stretching of the vibrations of aromatic ring (-C=C) was observed with a peak observed at 1630 cm^{-1} [36]. The C-S stretching was associated with the distinct band at 669 cm^{-1}. This gave an indication of sulfur-containing amino acids or metabolites involved in gold thiol chemistry contributing to AuNP stability [37]. Finally, absorption in the 600-500 cm^{-1} range, attributed to metal-ligand interactions. The appearance of peaks in this region for the AuNP sample indicates the formation of metal-organic bonds between gold and bacterial biomolecules confirming biomolecule functionalization on the AuNP surface [25,36] The peaks suggest that bacterial biomolecules, such as proteins, lipids, or polysaccharides, are involved in stabilizing AuNPs, with C-H and C-N/C-O groups forming a protective coating (Der et al., 2013). The biomolecular profile is consistent with bacterial synthesis both intracellular and extracellular (as verified by TEM images in Fig. 3), where proteins or polysaccharides assist to reduce Au^{3+}, cap the nanoparticles and assist in functionalization [29, 38].

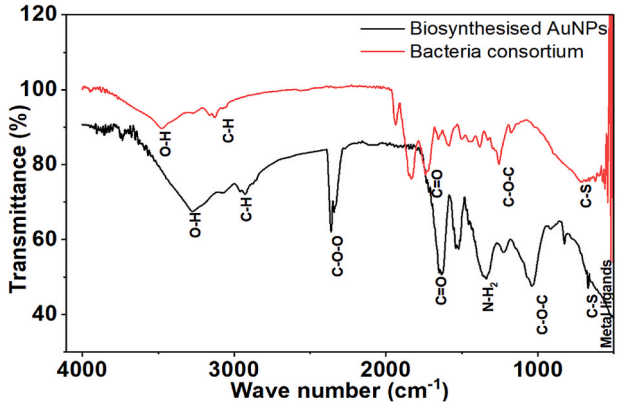

Fig. 5. FTIR spectrum of biosynthesized AuNPs as opposed to bacteria consortium.

In the AuNP spectrum, many of these functional groups were retained but exhibited reduced intensity or slight shifts, confirming their interaction with the nanoparticle surface (Fig. 5). For example, the C=O peak shifted and broadened, indicating binding of carbonyl groups to AuNPs, while the N–H band decreased in intensity, suggesting involvement of amine groups in capping. The presence of sulfur-containing biomolecules was confirmed by a pronounced band at 600 cm^{-1}. The C-S stretching indicated the role of residues in proteins such as cysteine in binding gold atoms [5]. The presence of hydroxylated and carbohydrate fractions in the form of O-H and C-O bands supports their role in nanoparticle stabilization [37]. Compared to the bacterial consortium, the AuNP spectrum exhibited generally lower transmittance

across most regions, particularly below 1500 cm^{-1}. Although the spectral profiles were similar in shape, they differed in intensity, with the AuNPs displaying broadened or shifted peaks. The results confirm the presence of bacterial metabolites on the surface of the gold nanoparticles (Fig. 5). The native biomolecular structure of AuNPs is retained, while the bacterial metabolites act as reducing and capping agents [39]. Proteins, polysaccharides, and sulfur-rich biomolecules secreted by the consortium appear to mediate the reduction of Au (III) to Au (0), while simultaneously stabilizing the resulting nanoparticles through effective capping interactions.

3.1.5. Crystallinity analysis via X ray diffraction (XRD)

The crystallographic properties of the biosynthesized gold nanoparticles were confirmed by X-ray diffraction (XRD) analysis (Fig. 6).

The crystallographic properties of biosynthesized gold nanoparticles (AuNPs) were described by X-ray diffraction analysis, as shown in Fig. 6. Distinct diffraction peaks were observed at 2θ values of approximately 38°, 44°, 64°, and 77°, corresponding to the (111), (200), (220), and (311) planes, respectively, of the face-centered cubic (FCC) lattice of gold [32]. These sharp, intense reflections confirm the high crystallinity of the AuNPs, with the (111) plane exhibiting the strongest intensity, indicative of a preferential orientation commonly observed in biologically synthesized AuNPs [40]. At approximately 28°, 55°, 80°, and 90°, minor diffraction peaks were observed. These were attributed to by-products generated during the biosynthesis process or residual biomolecular phases [41]. In line with FTIR evidence indicating biomolecular capping agents, presence of a broad background halo in Fig. 6 supports the involvement of organic components. Through organic surface interactions, bacterial metabolites play a crucial role in stabilizing AuNPs [42].

3.2. Application of AuNPs in water treatment

Biosynthesized AuNPs produced via consortium reduction were evaluated for their potential applications in water treatment. Antimicrobial properties and incorporation of AuNPs into composites for enhanced pollutant degradation were focus application areas.

3.2.1. Antimicrobial activity

Enterococcus spp. and *Klebsiella pneumoniae* were used as test pathogens for the antimicrobial activity of biosynthesized (AuNPs). The antimicrobial efficacy of AuNPs has been established against other bacterial indicators such as *E. coli* and Vibrio spp. [5,21,38]. However, data specific to Enterococcus spp. remains limited. *Enterococcus* is a critical fecal indicator bacterium for evaluating water quality. Its presence in distributed or source water signifies potential vulnerability to fecal contamination. In some settings, enterococci have been detected when *E. coli* was absent, revealing contamination that would be missed with coliform testing alone[43]. Because they often persist longer than *E. coli*, they can indicate more prolonged or upstream pollution whereas *E. coli* tends to reflect more recent fecal inputs[44]. *K. pneumoniae* is responsible for difficult-to- treat infections especially in hospitals such as pneumonia and urinary tract infections [45–47].

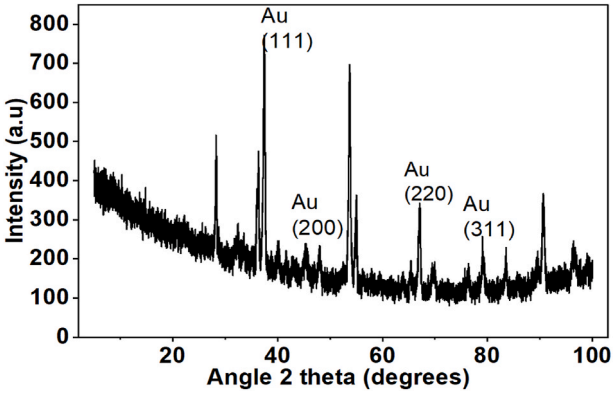

Fig. 6. X- Ray diffraction of biosynthesized AuNPs by bacteria consortium showing most prominent peaks observed at ~38.2°, 44.4°, 64.5° and 77.5°.

Results of Enterococcus showed that distinct inhibition zones were exhibited at concentrations of 25 μg/mL (12 mm inhibition diameter) and 50 μg/mL (19 mm inhibition diameter), in the well diffusion assay (Fig. 7a). Minimal or no activity was observed at lower concentrations (1 μg/mL and 5 μg/mL). 25 μg/mL penicillin produced a large inhibition zone (17 mm) pointing out the antibiotic's superior potency as a suitable control.

The growth curve analysis measured as optical density at 600 nm, OD_{600} (Fig. 7b), complemented the results from the well-diffusion assay. The results revealed a concentration-dependent reduction in *Enterococcus* spp. growth Fig. 7b. At 50 μg/mL the greatest growth inhibition of all 5 reactors was noted over 48 h. At 25 μg/mL, AuNPs suppressed growth without complete inhibition. The minimum inhibitory concentration (MIC) of the AuNPs against *Enterococcus* spp. lies between 5 and 25 μg/mL. Biologically synthesized nanoparticles against various bacteria have been reported within MIC ranges between 10–200 μg/mL [5,17]. Although the antimicrobial potency of AuNPs is lower than that of penicillin, their ability to inhibit growth at higher concentrations highlights their potential for use in antimicrobial coatings and as important aides in water treatment.

The growth curve in Fig. 7d revealed that *K. pneumoniae* underwent a lag phase lasting 3-4 h before entering exponential growth, ultimately reaching and maintaining stationary phase beyond 30 h. The gold nanoparticles demonstrated significant bacteriostatic activity during the initial 16-h period as shown by the well diffusion Fig. 7c. They inhibited proliferation of the bacteria in a dose-dependent manner with distinct inhibition zone significant for 25 μg/mL (12.5 mm inhibition diameter) and 50 μg/mL (18 mm inhibition diameter). There was visible minimum proliferation of colonies rather than complete inhibition on the 1 μg/mL and 5 μg/mL wells as shown in Fig. 7c. However, this inhibitory effect diminished over time, with complete bacterial colonization observed across the well diffusion plates by 24 h, indicating bacterial regrowth at the different concentrations. This aligns with established findings that gold nanoparticles at concentrations below bactericidal thresholds delay rather than completely eliminate bacterial growth cycles [18,48]. These results emphasize that both the concentration of AuNPs and the frequency of dosing are critical determinants of sustained antimicrobial efficacy against multidrug-resistant *K. pneumoniae* [49]. The observed regrowth suggests that maintaining therapeutic concentrations through repeated dosing may be necessary to achieve complete bacterial eradication rather than temporary growth suppression. These properties suggest potential applications in combating pathogens, particularly in environmental remediation and medical contexts, though further testing against specific bacterial strains would refine their efficacy.

3.2.1.1. Mechanisms of antimicrobial activity. Further analysis to support the multiple antimicrobial mechanisms of biosynthesized AuNPs against bacteria is outlined in this section. These include.

3.2.1.1.1. Hydrophobicity. Hydrophobic interactions, as identified by FTIR results (Fig. 5) showing peaks at 2922 cm^{-1} and 1338 cm^{-1} indicative of C–H and aromatic C=C stretching, enhance AuNP interactions with bacterial cell membranes, particularly the lipid bilayers of Gram-negative bacteria [3,5,21,50]

Fig. 8 shows the TEM image revealing AuNPs associating with cell membranes, leading to destabilization and rupture. Despite the thick peptidoglycan layer of Gram-positive bacteria, the hydrophobic and charged groups on AuNPs alter membrane potential and inhibit ATP synthase activity, likely due to electrostatic attraction between the nanoparticles and negatively charged bacterial cell walls [3,5,21,50].

3.2.1.1.2. Biofilm inhibition and surface chemistry interactions. Apart

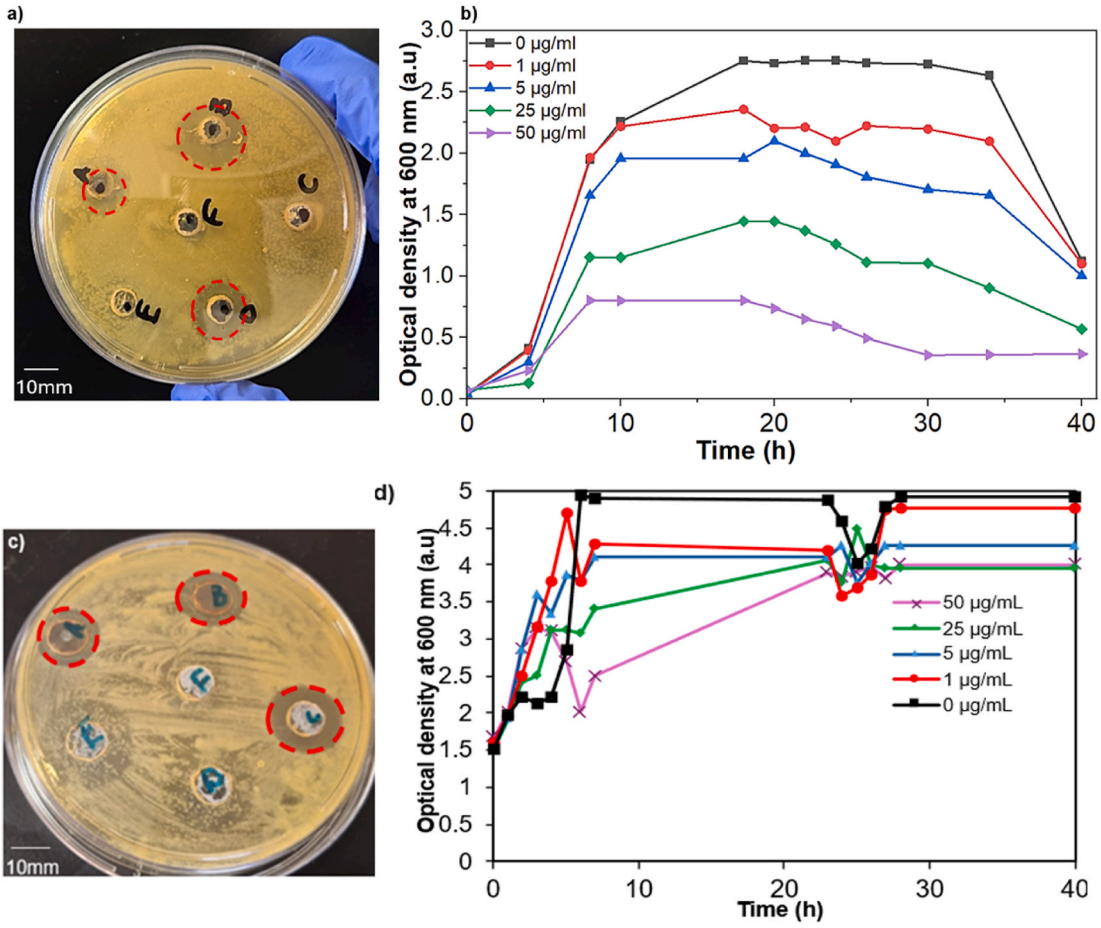

Fig. 7. a) Well-diffusion assay results for *Enterococcus* after 24 h: A (25 µg/mL AuNPs), B (50 µg/mL AuNPs), C (deionized water), D (25 µg/mL) penicillin), E (5 µg/mL AuNPs) and F (1 µg/mL). b) Growth of *Enterococcus* spp. in the presence of varying concentrations (0-50 µg/mL) of AuNPs. c) Well-diffusion assay results after 16 h for *K. pneumoniae* A (25 µg/mL AuNPs), B (50 µg/mL AuNPs), C (25 µg/mL) penicillin), D (5 µg/mL AuNPs), E (1 µg/mL) and F (deionized water) d) Growth of *K. pneumoniae* in the presence of varying concentrations (0-50 µg/mL) of AuNPs.

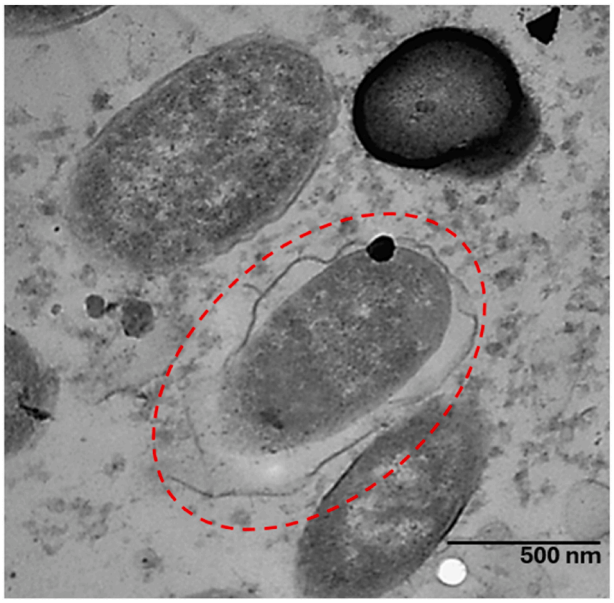

Fig. 8. AuNP attached to the surface of the bacteria and disrupting the membrane structure.

from disrupting the membrane, the hydrophobic surfaces can limit biofilm formation by reducing bacterial adhesion. Reduced biofilm formation is also a result of surface chemistry slowing down initial bacterial adhesion to surfaces [42]. Bacterial extracellular polymeric substances modulate these interactions thereby reducing biofilm maturation. The stabilizing coating imparts a slight positive or negative charge to the AuNPs. This coating is derived from proteins or polysaccharides, as evidenced by FTIR in Fig. 5 corresponding to C-N and C-O groups. Positively charged AuNPs particularly those featuring amine groups electrostatically interact with negatively charged bacterial cell walls such as lipopolysaccharides in Gram-negative bacteria or teichoic acids in Gram-positive ones[18,42]. This enhanced binding promotes antimicrobial efficacy against diverse pathogens, including gram-positive and gram-negative bacteria. Improved adhesion to negatively charged bacterial membranes is necessitated by amine groups on positively charged surfaces. This enhances antimicrobial activity against multi-drug resistant (MDR) strains as there is improved binding to negatively charged bacterial membranes [3,21].

3.2.1.1.3. Oxidative stress and cell membrane integrity. Cell wall and membrane disruption was due to accumulation of gold nanoparticles within bacterial cells. Release of cellular contents following cell membrane rupture was observed in TEM images (Fig. 9a and b). Oxidative stress induced by the generation of reactive oxygen species (ROS) mediates this process, as supported by Duman and Akda [21].

Critical cellular components, including proteins, lipids, and DNA are oxidized when ROS levels are elevated. This leads to inhibition of bacterial replication and other metabolic processes. This intensifies cellular damage as the imbalance may overwhelm bacterial antioxidant

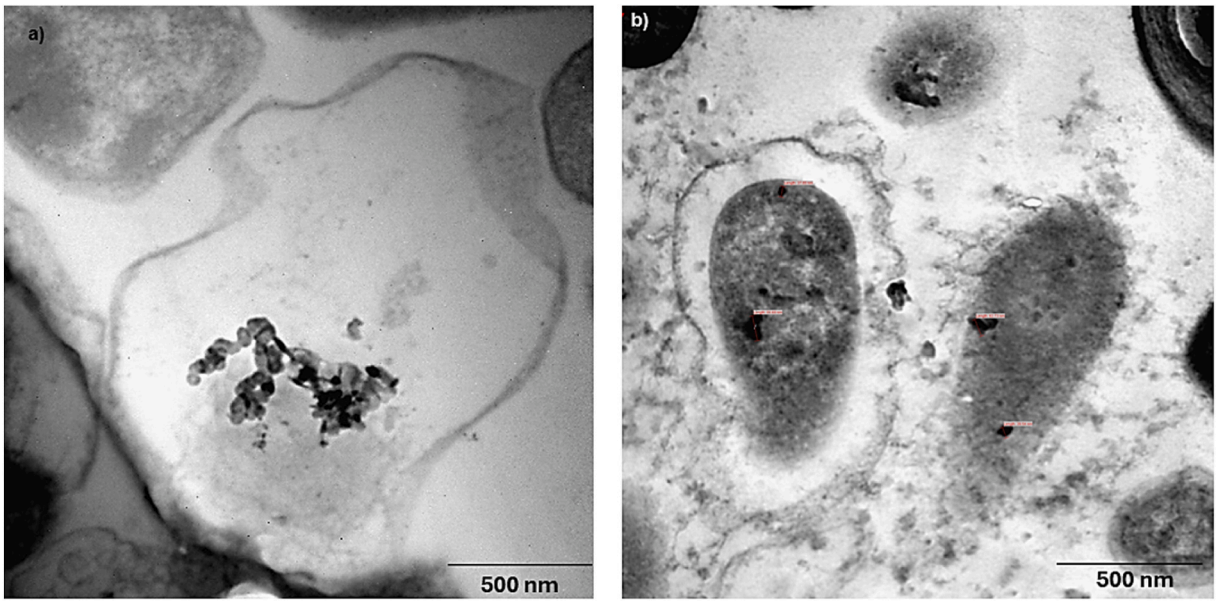

Fig. 9. a) AuNPs accumulating inside the bacterial b) AuNPs inside the cell and on the cell membrane, with cells showing loss of membrane integrity.

defenses. AuNPs bind to sulfur-containing enzymes using C–S stretching (400–600 cm^{-1} of FTIR, Fig. 5) disrupting respiratory chains. This worsens cellular dysfunction and leads to cell death due to increased ROS production [38].

Fig. 10 showed that AuNP accumulation caused cell rupture, releasing both nanoparticles and cellular contents. AuNP accumulation stimulates ROS production, compromising mitochondrial and plasma membrane integrity [51]. The resulting oxidative stress and mitochondrial dysfunction lead to necrosis, characterized by loss of membrane integrity and release of nanoparticles with cellular debris [52,53].

3.2.2. *Photocatalytic degradation of rhodamine B dye*

Photocatalytic degradation of Rhodamine B (RhB), a common organic dye pollutant, can be achieved using TiO_2 Degussa (P25), under UV light. Studies have shown that TiO_2 can degrade 14.6 % RhB in 2 h and 60.69 % under UV [54]. This material has a bandgap of approximately 3.0-3.2 eV and generates electron-hole pairs, facilitating the oxidative breakdown of RhB into harmless byproducts [55]. To enhance its photocatalytic properties, Degussa TiO_2 was combined with bio-synthesized AuNPs.

3.2.2.1. Photocatalytic degradation performance under visible light. Fig. 11 (a) describes the normalized concentration (C/C_0) of a RhB over time under visible light irradiation for photolysis, pure TiO_2, and TiO_2 modified with 0.5 wt% AuNPs. The experiment included an initial dark period (light off) followed by visible light exposure (light on). There was minimal to negligible degradation under photolysis, with C/C_0 remaining near 1.0 after 300 min. Pure TiO_2 exhibited limited degradation, reducing C/C_0 to approximately 0.4, (approximately 12.8 % degradation after 120 min and approximately 62 % after 6 h of irradiation). This poor visible light activity was likely due to its wide band gap of 3.1 eV [54]. In contrast, TiO_2/0.5 wt% AuNPs demonstrated significantly enhanced degradation, lowering C/C_0 to about 0.2 within 300 min (23.5 % in first 120mins and approximately 76 % after 6 h).

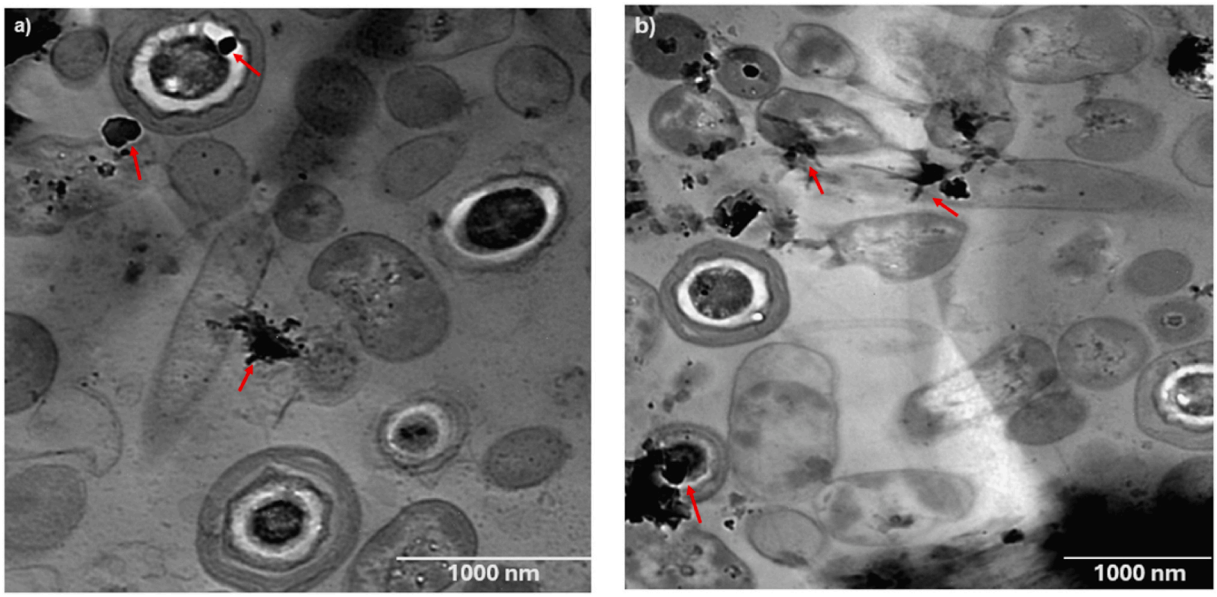

Fig. 10. a), b) Presence of AuNPs inside of cells leading to cell rupture and releasing of cell contents.

This improvement is attributed to the incorporation of AuNPs. The presence of AuNPs extended the light absorption of TiO_2 into the visible region through localized surface plasmon resonance (LSPR)[13,21]. This enhanced charge separation and promoted the generation of reactive oxygen species (ROS) [5]. To facilitate greater electron transfer and ROS production, Neama [24] suggested higher AuNP loading to increase the LSPR effect.

3.2.2.2. Photocatalytic degradation performance under sunlight. As presented in Fig. 11 (c), in the absence of a catalyst (photolysis), minimal degradation occurs, with C/C_0 remaining close to 1.0 throughout, suggesting negligible direct photodecomposition of the pollutant under sunlight. Pristine TiO_2 showed moderate degradation, with C/C_0 decreasing to approximately 0.2 after 200 min (approximately 39 % RhB degradation after 120 min). This showed improved photocatalytic activity than in Fig. 11 (a) due to solar irradiation. TiO_2/0.5 wt% AuNPs outperformed pristine TiO_2, achieving near-complete degradation C/C_0 at less than 0.05 after the same 200 min (approximately 91 % RhB removal). This enhancement is attributed to the plasmonic effects of AuNPs, which extend light absorption into the visible region (as evidenced by UV-Vis DRS data in subsequent sections). Photocatalytic efficiency under solar irradiation was improved due to charge separation and extended light absorption ([56], Yasumoto, Imai, & Sakamoto, 2017).

3.2.2.3. Kinetic analysis. The pseudo-first-order kinetic plots are shown as $\ln(C_0/C)$ versus time for the photocatalytic degradation of a target pollutant. Fig. 11(b) presents under visible light while 11(d) shows under sunlight for both TiO_2 and TiO_2/0.5 wt% AuNPs. High correlation coefficients were obtained $R^2 = 0.96$ for TiO_2 and $R^2 = 0.95$ for TiO_2/0.5 wt% AuNPs under visible light, and $R^2 = 0.92$ for TiO_2 and $R^2 = 0.98$ for TiO_2/0.5 wt% AuNPs under sunlight. Both datasets confirmed first-order kinetics and values validated the kinetic model's applicability.

Fig. 11b under visible light, shows the rate constant (k) for TiO_2/0.5 wt% AuNPs of approximately 0.0025 min^{-1}, compared to 0.0015 $min^{-1}$for pure TiO_2, (1.67-fold increase). Fig. 11d under sunlight shows the rate constant for TiO_2/0.5 wt% AuNPs rises to about 0.019 min^{-1}, a 2.5-fold improvement over TiO_2's 0.0075 min^{-1}. This enhanced rate under sunlight reflects the utilization of broader spectral due to AuNPs' SPR, which extends absorption into the visible range. It is further amplified by UV contributions in sunlight. The steeper slopes for TiO_2/0.5 wt% AuNPs in both conditions highlight the role of AuNPs in facilitating hot electron injection and reducing electron-hole recombination via the Schottky barrier at the TiO_2-Au interface [57]. These kinetic improvements explain the superior photocatalytic efficiency of the modified catalyst across different light sources.

3.2.2.4. Recyclability of gold doped TiO_2. The recyclability of the TiO_2/0.5 wt% AuNPs photocatalyst over three cycles under sunlight is shown Fig. 12. Degradation percentages were 98.96 %, 95.35 %, and 90.67 % respectively.

Fig. 12 indicates a high initial photocatalytic performance, with a gradual decline of 3.61 % from cycle 1 to cycle 2. A decrease of 4.68 % from cycle 2 to cycle 3, totaling a 8.29 % reduction was noticed after three cycles. The consistent high efficiency suggests that the gold-doped TiO_{22} retains substantial photocatalytic activity and structural stability, likely due to the stabilizing effect of AuNPs [58]. The slight decrease may be attributed to minor catalyst loss, surface fouling, or active site deactivation during recycling, but the material remains highly recyclable and effective for repeated use in photocatalytic applications. This indicates excellent recyclability, as the catalyst maintains high degradation efficiency (>90 %) even after three cycles. After the 3 cycles, the

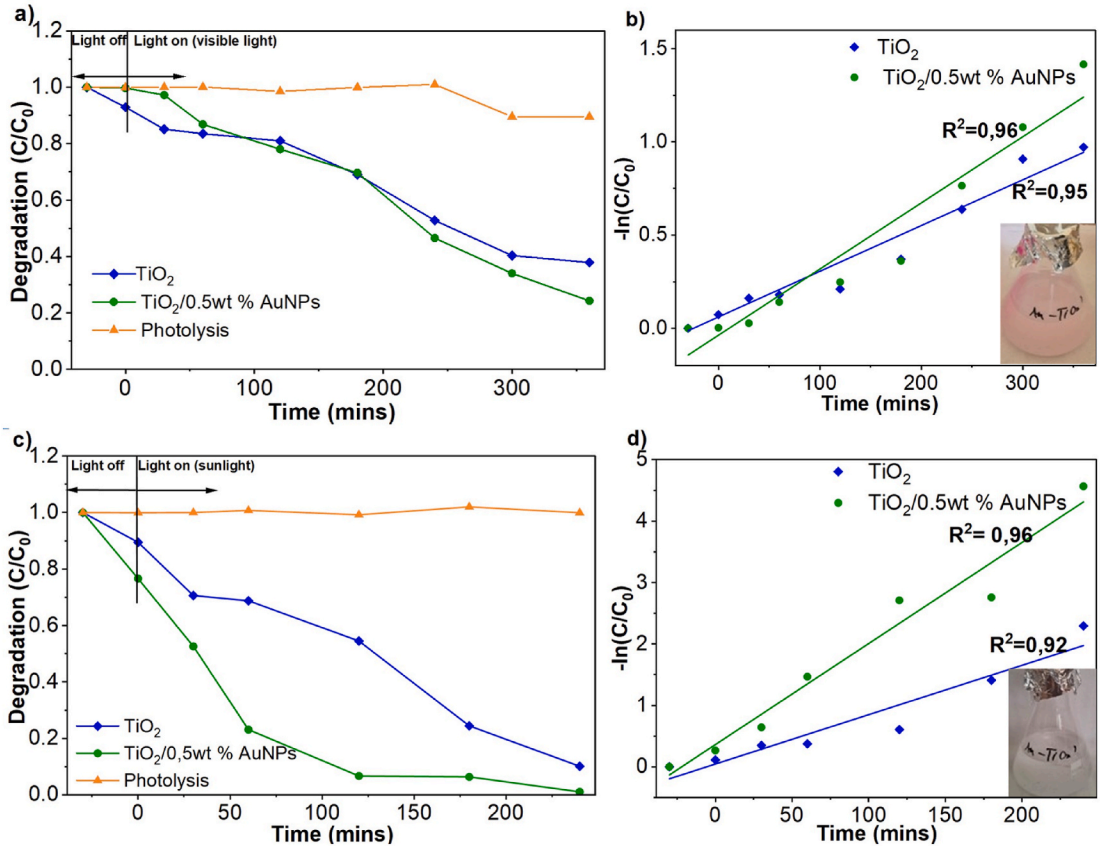

Fig. 11. Results showing the degradation of 10 ppm RhB dye in 360 min under a) visible light b) sunlight, with exposure time. Corresponding linear fitting of -ln (C/C_0) Pseudo-First-Order Kinetic Plots (with final state of dye after 4 h shown as inserts) under c) visible light and d) sunlight exposure.

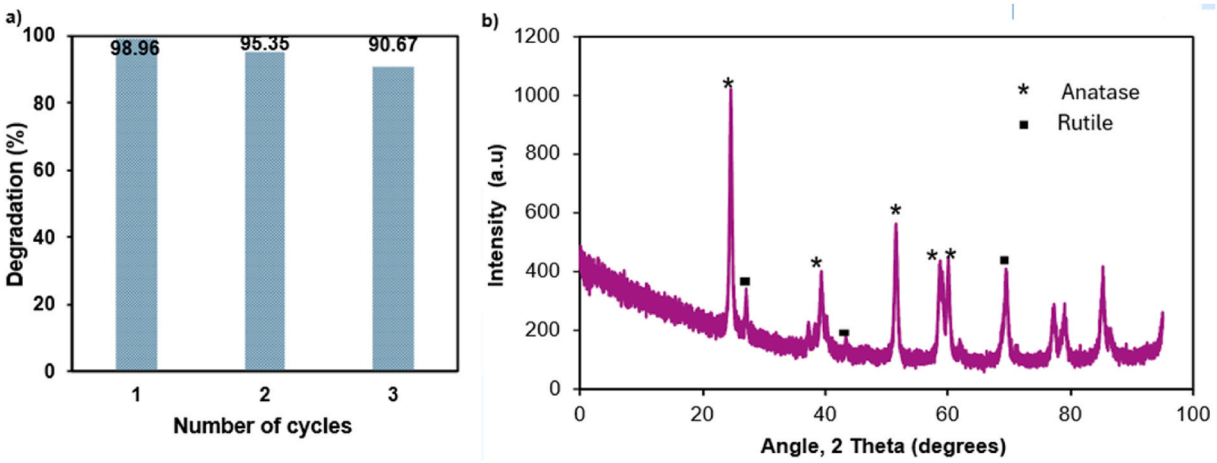

Fig. 12. a). Recycling and reusability in 3 cycles of TiO_2/0.5 wt% AuNPs for photocatalytic degradation of RhB under sunlight. b) XRD of TiO_2/0.5 wt% AuNPs after 3 cycles of degradation.

XRD showed some changes in the peaks of the composite. While the ratio for the two phases anatase/rutile ratio remained constant (Fig. 12b), there was an increase in the intensity peak for the composite. This showed structural stability and hence the slight decline in performance (from 98.96 % to 90.67 %) suggests minor deactivation. This was possibly due to the accumulation of intermediates, loss of active sites, or slight leaching of Au nanoparticles [58,59]. Other regeneration methods such as thermal or chemical cleaning can further enhance its reusability, making AuNP- doped TiO_2 a cost-effective and sustainable option for environmental remediation.

3.2.2.5. Comparative characterization of pure TiO_2 (Degussa P25) and Au doped TiO_2. A comparative characterization was conducted to evaluate the structural and physicochemical differences between pure TiO_2 (Degussa) and its Au-doped counterpart, aiming to assess enhancements in photocatalytic performance. Degussa TiO_2 comprises an anatase (85%) and rutile (15%) phase composition, with an average crystallite size of 20–30 nm and a specific surface area of ~54 m^2/g. In this study, biosynthesized AuNPs were incorporated into Degussa TiO_2 to augment its photocatalytic properties.

3.2.2.5.1. Crystallinity differences

Particle size and morphology

SEM images were taken to analyze both morphology and particle size before and after Au doping (Fig. 13).

SEM images assessed the morphological and particle size differences between pristine TiO_2 (Degussa) and Au-doped TiO_2 composites, synthesized per Section 2.5. The SEM micrograph of pristine TiO_2 (Fig. 13a) shows a compact, agglomerated structure with irregular, densely packed nanoparticle clusters, exhibiting limited porosity and a rough texture, consistent with a 20–30 nm crystallite size from XRD. In contrast, the Au-doped TiO_2 micrograph (Fig. 13b) reveals a heterogeneous, loosely packed morphology with increased porosity and interparticle voids, attributed to AuNPs acting as heterogeneous nucleation sites on activated TiO_2. As detailed in section 2.5 enhanced AuNP dispersion was achieved by pH adjustment to 4-5, heating to 60 °C, and calcination at 300 °C. This likely improved photocatalytic efficiency as it resulted in smaller particle sizes and higher surface area, via enhanced charge separation and active site availability [60].

Surface functional groups via FTIR and crystallinity via XRD

FTIR showed the differences in surface bonds while XRD was used to analyze the crystallinity of the two materials as shown in Fig. 14a) and b). Minimal surface defects on the surface of highly crystalline pure TiO_2 (Fig. 14a) were demonstrated. Enhanced defect density with increased surface irregularities in the region between 700 and 1200 cm^{-1} were indicated on the Au-doped. These defects improved catalytic efficiency as they exposed more reactive edge sites and facilitated improved electron transfer pathways as confirmed by Rahulan [61]. The plasmonic properties of incorporated AuNPs contributed to enhanced visible-light absorption and improved charge separation, creating synergistic effects for overall photocatalytic performance [13].

Fig. 14b) revealed X-ray diffraction analysis highlighting significant structural modifications before and after AuNP incorporation into the TiO_2 matrix. The peaks of anatase were strongest at approximately 25° (101 plane) with other weaker peaks at 38°, 48°, 54° and 63°. A weak

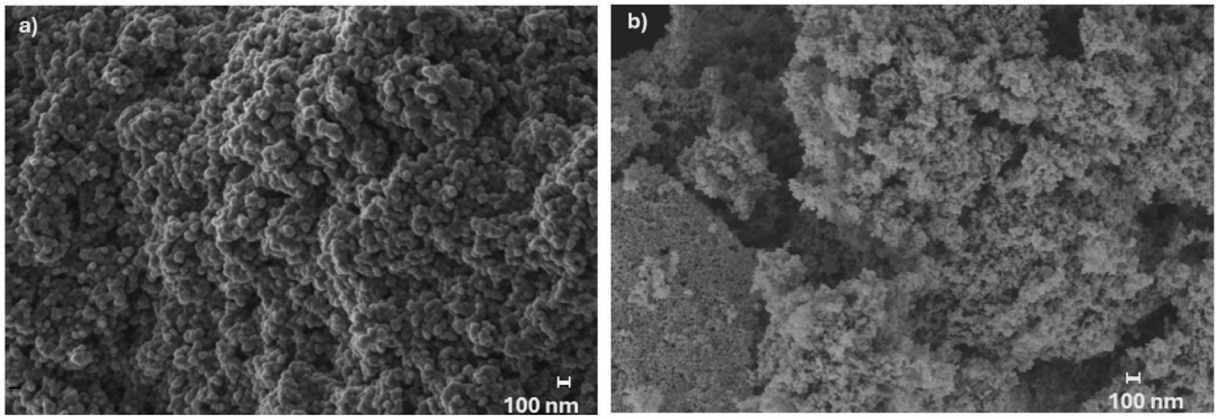

Fig. 13. SEM images at 50,000x magnification showing morphology and particle size of TiO_2 a) before Au doping and b) after Au doping.

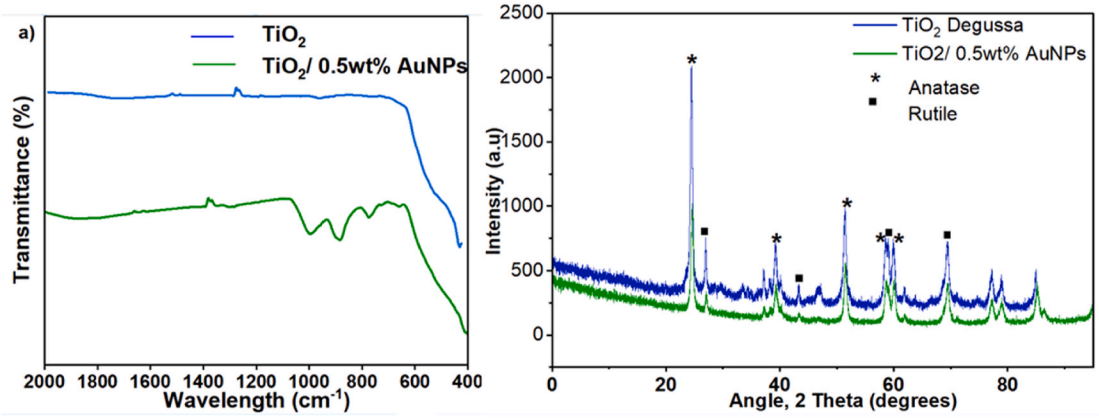

Fig. 14. Comparison of a) Surface functional groups of pure TiO_2, Degussa and TiO_2/0.5 wt% AuNPs composite b) Crystallinity of pure TiO_2, Degussa and TiO_2/0.5 wt% AuNPs composite.

peak of rutile was also showing at 27° (110 plane), 36° and 54° [62,63]. Reduced peak intensities were noted in the Au-doped TiO_2 composite (Fig. 14b) indicative of decreased crystallinity and smaller crystallite sizes. This suggested increased structural disorder and the introduction of defects within the crystal lattice of the formed composite. This likely arose from the incorporation of AuNPs at grain boundaries and within the TiO_2 framework. More active sites and surface area availability are created by these structural changes [60]. Au doping presents an

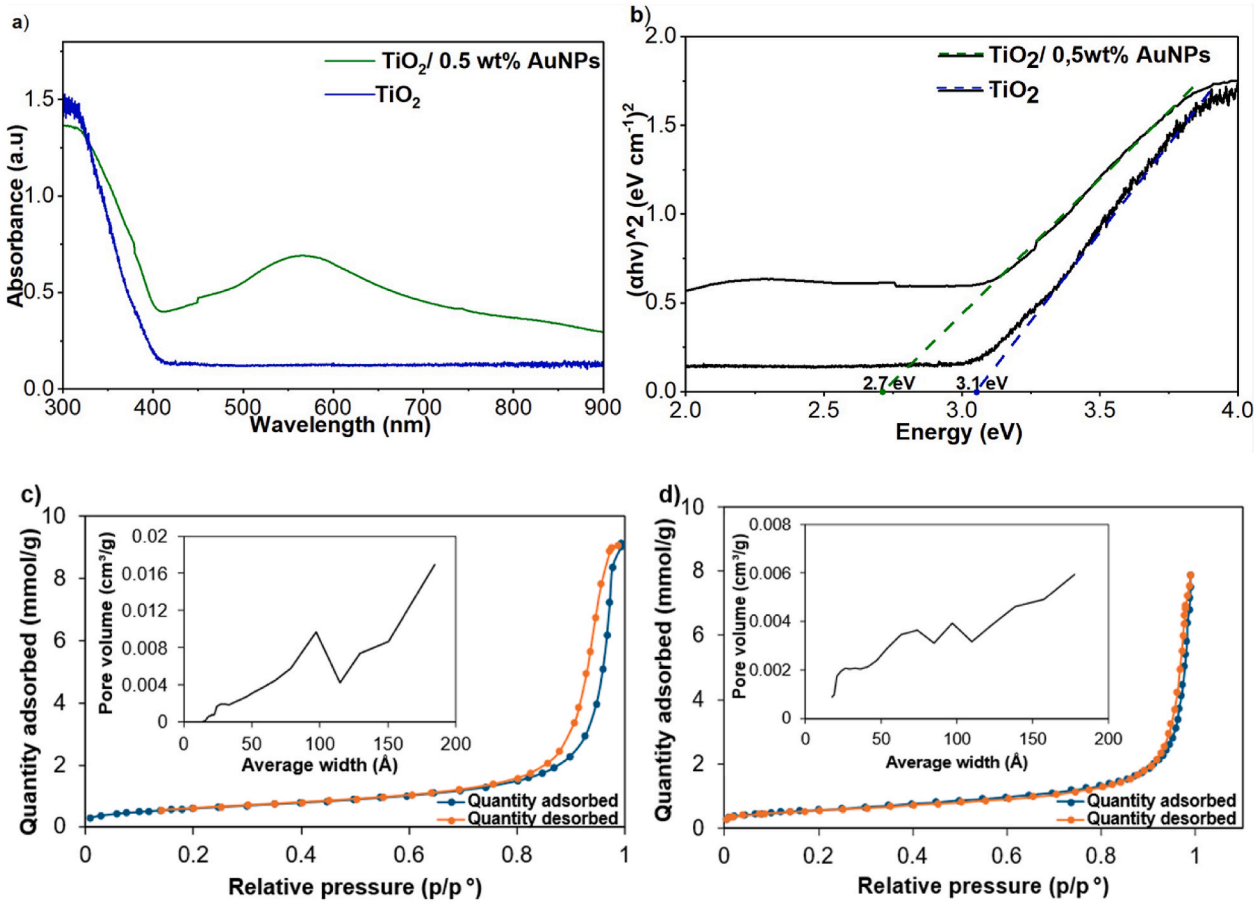

e)

Adsorbent	BET surface area	Pore volume	Adsorption pore width
TiO_2/0.5wt%AuNPs	47.6189m²/g	0.011377 cm³/g	61.708 Å
TiO_2	46.3726 m²/g	0.228162 cm³/g	50.415 Å

Fig. 15. a) UV Vis DRS absorbance of TiO_2 and TiO_2/0.5% wt AuNP b) Tauc's plot for band gap determination of TiO_2 and TiO_2/0.5% wt AuNP. Nitrogen Adsorption-Desorption Isotherms and Pore-Size Distribution Curves (inserts) of (c) TiO_2/0.5 wt% AuNPs and (d) TiO_2, with Comparative Physical Properties in (e).

advantageous and deliberate introduction of defects that are necessary to catalytic performance.

BET and bandgap of pure TiO_2 and TiO_2/0.5 wt% AuNP

Absorption behaviors between TiO_2 and TiO_2/0.5 wt% AuNPs were analyzed via UV-Vis DRS absorbance spectra (Fig. 15a). A distinct peak for TiO_2 emerged around 400 nm, consistent with its wide band gap. As for TiO_2/0.5 wt% AuNPs, it showed enhanced absorption in the visible region (400–800 nm), attributed to the SPR effect of AuNPs. This explains the enhanced photocatalytic activity under visible light as the presence of AuNPs improved light harvesting potential.

From Tauc plots in Fig. 15b, the band gap energies were derived. TiO_2 revealed a band gap of approximately 3.1 eV for and 2.7 eV for TiO_2/0.5 wt% AuNPs composite. There was a shift toward visible light activity facilitated by AuNP-induced electron transfer. Mesoporous structures were confirmed by the nitrogen adsorption-desorption isotherms and pore-size distributions in Fig. 15 c) and d). An average pore width of TiO_2/0.5 wt% AuNPs was reported as 61.708 Å, compared to 50.415 Å for TiO_2 (Fig. 15e). The composite also reported a higher BET surface area (47.6189 m^2/g vs. 46.3726 m^2/g) and pore volume (0.011377 cm^3/g vs. 0.228162 cm^3/g) compared to pristine TiO_2. This indicated enhanced textural properties in the Au doped composite.

The nitrogen adsorption-desorption isotherms (Fig. 15c and d) for both samples exhibit Type IV isotherms with H3 hysteresis loops, indicative of mesoporous materials. The pore-size distribution curves (inserts) confirm a narrow pore size distribution, with average pore widths of 61.708 Å for TiO_2/0.5 wt% AuNPs and 50.415 Å for TiO_2. The increased pore width in the AuNP-modified sample may enhance mass transport and accessibility of active sites.

Comparative physical properties (Fig. 15e) show that TiO_2/0.5 wt% AuNPs have a slightly higher BET surface area (47.6189 m^2/g) and pore volume (0.011377 cm^3/g) compared to TiO_2 (46.3726 m^2/g and 0.228162 cm^3/g, respectively). Additional surface and porosity parameters are detailed in Supplementary material S1.1 and S1.2. This improvement suggests that AuNP incorporation may refine the mesoporous structure, potentially boosting adsorption capacity and catalytic performance. Overall, the incorporation of 0.5 wt% AuNPs into TiO_2 enhances visible light absorption, reduces the band gap, and improves textural properties, making it a promising material for photocatalytic applications [55].

Though the composite had the reduced pore volume, the increased surface area and larger pore width of TiO_2/0.5 wt% AuNPs likely contributed to its enhanced catalytic performance. These features facilitated better surface interactions and charge dynamics, aligning with the observed structural defects explained prior in Fig. 14.

3.2.2.6. Effect of adding AuNPs to TiO_2 on surface plasmon resonance (SPR). Addition of AuNPs to TiO_2 introduced plasmonic effects that gave rise to absorption band in the visible range (500-600 nm) [64,65]. This extended the light harvesting beyond the UV range of pristine TiO_2, likely due to interfacial electronic coupling. The AuNPs addition also led to an apparent reduction in the band gap from 3.1 to 2.7 eV (Fig. 15a) consistent with the study by Ahmad et al. [66]. This was possibly due to absorption enhancement, interfacial charge transfer, and the formation of localized electronic states. The Au- TiO_2 junction facilitates bidirectional charge transfer, acts as an electron sink where AuNPs trap photoexcited electrons from TiO_2 under UV light. This reduces electron-hole recombination under UV light. Under visible light, the reverse occurs via hot-electron injection. SPR also induces intense localized electromagnetic fields (plasmonic hotspots). This amplifies light absorption in adjacent TiO_2 areas accelerating surface reactions.

Fig. 16 compares the possible photocatalytic mechanisms by pure TiO_2 (a) and AuNP doped TiO_2 (b). Pure TiO_2 is sufficiently activated under UV irradiation generating electron-hole pairs. However, its photocatalytic efficiency is limited by rapid charge recombination before the electrons reach the surface. This leads to significant energy loss and the formation of only a small amount of reactive species for degradation of the dye. In contrast, Au-doped TiO_2 can utilize both UV and visible light. Addition of gold nanoparticles enhanced TiO_2 photocatalysis through surface plasmon resonance significantly modifying TiO_2's optical, photocatalytic and textural properties. This was possibly by enabling visible-light sensitization via hot-electron injection across the Au-TiO_2 Schottky barrier [67]. This shifted absorption and narrowed the band gap from approximately 3.1 eV to 2.7 eV due to interfacial electronic coupling and mid-gap state formation. The metal-semiconductor

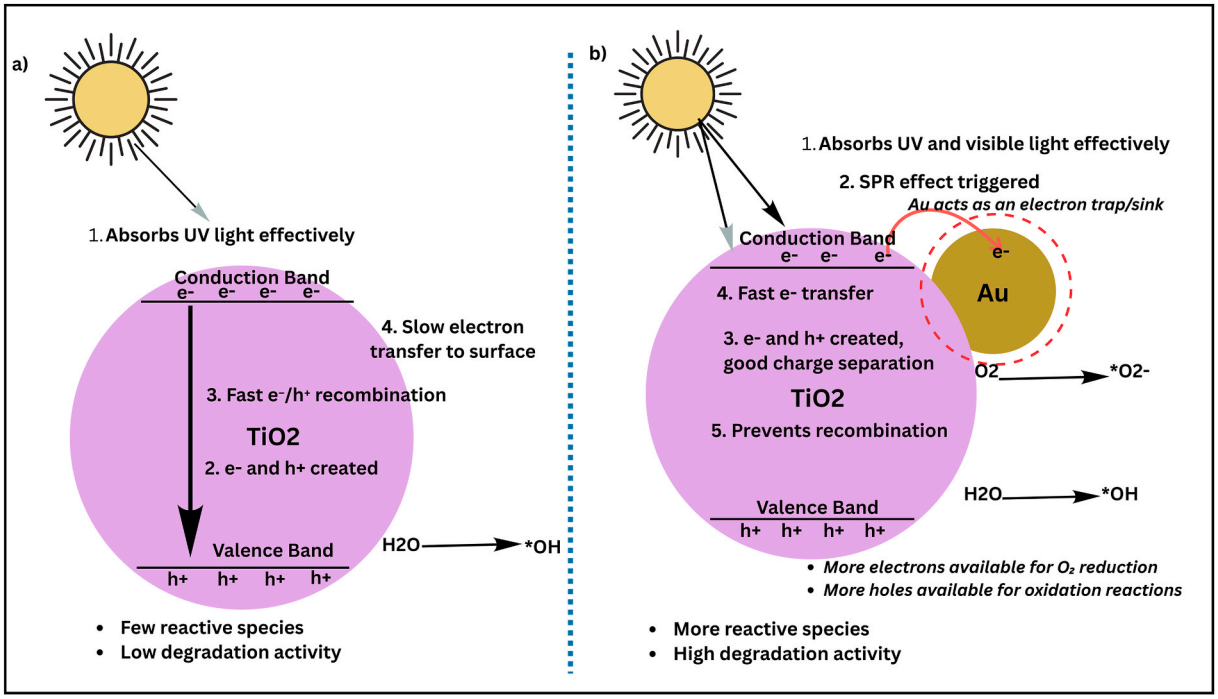

Fig. 16. Comparison of photocatalytic mechanisms in pure TiO_2 and Au-doped TiO_2 highlighting the role of Au-induced surface plasmon resonance (SPR) in visible-light absorption, charge separation, and enhanced reactive species generation.

junction facilitated two-directional charge transfer [62]. Firstly, by trapping photoexcited electrons from TiO_2 under UV illumination [68]. Secondly, injecting plasmonic hot electrons into the conduction band under visible light thereby suppressing electron-hole recombination and improving quantum efficiency [56]. Additionally, SPR generated intense localized electromagnetic fields that amplified light absorption in adjacent TiO_2 regions [69]. This accelerated surface reactions, while the AuNPs' presence modified the catalyst's morphology by altering porosity and surface area through partial pore blocking. Simultaneously, thermal and photochemical stability were enhanced by preventing phase transformations and sintering.

4. Conclusion

The biosynthesis by bacterial consortium produced biomolecular capped and partially agglomerated AuNPs. They were predominantly spherical with size ranges between 20 and 125 nm. These nanoparticles showed dose-dependent inhibition of *Enterococcus* spp., with strongest suppression at 50 μg/mL and minimal effects at 1 μg/mL. The antimicrobial activity was linked to membrane damage, ROS generation, and growth prevention due to AuNP presence. When combined with TiO_2 for photocatalysis, 0.5 wt% AuNP-doped TiO_2 composite achieved 98.96 % Rhodamine B degradation under sunlight, outperforming pure TiO_2. It also showed great reusability after retaining >90 % efficiency across three cycles. This was attributed to enhanced surface area and defect-assisted charge dynamics. These results demonstrated the potential use of consortium-mediated AuNPs in antimicrobial activity and pollutant removal in water. Future studies should explore different synthesis conditions and media for AuNPs and assess antimicrobial activity of AuNPs against multidrug-resistant pathogens. Future investigations will determine interfacial charge transfer mechanisms of AuNP/TiO_2 to advance application-specific design. Additionally, time-resolved photoluminescence spectroscopy can be explored to quantify charge carrier lifetimes for the Au/TiO_2 composite. In situ photocurrent measurements under monochromatic illumination will be needed to isolate SPR contributions.

Data availability statement

The data that support the findings of this paper are openly available in University of Pretoria Research Data Repository.

Funding

The authors received financial support for the research, partially from the National Research Fund (NRF) South Africa through Grant numbers: SRUG2204072544 and CSRP23042396323 awarded to Prof Shepherd Tichapondwa and Prof Evans Chirwa as well as the Margaret McNamara Education Grant of 2025 awarded to Miranda Mpeta.

CRediT authorship contribution statement

Miranda Mpeta: Conceptualization, Formal analysis, Investigation, Methodology, Writing – original draft, Writing – review & editing. **Job T. Tendenedzai:** Writing – original draft, Writing – review & editing. **Shepherd M. Tichapondwa:** Funding acquisition, Resources, Supervision, Writing – review & editing. **Evans M.N. Chirwa:** Funding acquisition, Resources, Supervision, Writing – review & editing.

Declaration of competing interest

The authors declare that they have no known competing financial interests or personal relationships that could have appeared to influence the work reported in this paper.

Appendix A. Supplementary data

Supplementary data to this article can be found online at https://doi.org/10.1016/j.mtsust.2026.101333.

Data availability

Data will be made available on request.

References

[1] S. Chaturvedi, P.N. Dave, N.K. Shah, Applications of nano-catalyst in new era, J. Saudi Chem. Soc. 16 (3) (2012) 307–325, https://doi.org/10.1016/j.jscs.2011.01.015.
[2] F.D. Guerra, M.F. Attia, D.C. Whitehead, F. Alexis, Nanotechnology for environmental remediation: materials and applications, Molecules 23 (7) (2018) 1–23, https://doi.org/10.3390/molecules23071760.
[3] V. Ramalingam, Multifunctionality of gold nanoparticles: plausible and convincing properties, Adv. Colloid Interface Sci. 271 (2019) 101989, https://doi.org/10.1016/j.cis.2019.101989.
[4] S.K. Das, A.R. Das, A.K. Guha, Gold nanoparticles: microbial synthesis and application in water hygiene management, Langmuir 25 (14) (2009) 8192–8199, https://doi.org/10.1021/la900585p.
[5] S. Yougbare, T.K. Chang, S.H. Tan, J.C. Kuo, P.H. Hsu, C.Y. Su, T.R. Kuo, Antimicrobial gold nanoclusters: recent developments and future perspectives, Int. J. Mol. Sci. 20 (12) (2019), https://doi.org/10.3390/ijms20122924.
[6] A.L. Campaña, A. Saragliadis, P. Mikheenko, D. Linke, Insights into the bacterial synthesis of metal nanoparticles, Front. Nanotechnol. 5 (August) (2023) 1–20, https://doi.org/10.3389/fnano.2023.1216921.
[7] Y. Liu, X. Wang, Colorimetric speciation of Cr (III) and Cr (VI) with a gold nanoparticle probe, Anal. Methods 5 (6) (2013) 1442–1448, https://doi.org/10.1039/c3ay00016h.
[8] M.Y. Abubakar, A.B. Adam, R. Shamsuddeen, T.S. Mathew, Environmental remediation using nanoparticles: a review, Kwaghe International Journal of Science and Technology (2024), https://doi.org/10.58578/KIJST.v1i1.3622. July.
[9] P. Parameswari, N. Belagalla, B.V. Singh, G. Abhishek, G. Rajesh, D. Katiyar, B. Hazarika, S. Paul, Nanotechnology-based sensors for real-time monitoring and assessment of soil health and quality: a review, Asian Journal of Soil Science and Plant Nutrition 10 (2) (2024) 157–173, https://doi.org/10.9734/ajsspn/2024/v10i2272.
[10] A. Shah, S. Akhtar, F. Mahmood, S. Urooj, A.B. Siddique, M.I. Irfan, M. Naeem-ul-Hassan, M. Sher, A. Alhoshani, A. Rauf, H.M.A. Amin, A. Abbas, *Fagonia arabica* extract-stabilized gold nanoparticles as a highly selective colorimetric nanoprobe for Cd^{2+} detection and as a potential photocatalytic and antibacterial agent, Surf. Interfaces 51 (2024) 1–11, https://doi.org/10.1016/j.surfin.2024.104556.
[11] Y. Tang, Y. Li, P. Chen, S. Zhong, Y. Yang, Nucleic acid aptamer-based sensors for bacteria detection: a review, Bioessays 47 (3) (2025) 1–33, https://doi.org/10.1002/bies.202400111.
[12] Y. Wu, Q. Yu Liu, Z. Qi Bu, M. Xia Quan, J. Yang Lu, W. Tao Huang, Colorimetric multi-channel sensing of metal ions and advanced molecular information protection based on fish scale-derived carbon nanoparticles, Spectrochimica Acta - Part A: Molecular and Biomolecular Spectroscopy 290 (2023) 1–10, https://doi.org/10.1016/j.saa.2022.122291.
[13] M. Gul, M. Kashif, S. Muhammad, S. Azizi, H. Sun, Various methods of synthesis and applications of gold-based nanomaterials: a detailed review, Cryst. Growth Des. (2025), https://doi.org/10.1021/acs.cgd.4c01687.
[14] M. Baserisalehi, M. Ahmadi, Parivash Ghaderinia, Biological synthesis of nanoparticles using bacteria, Journal of Advances in Biology 9 (4) (2017) 2027–2032, https://doi.org/10.24297/jab.v9i4.5676.
[15] A.B. Siddique, M.A. Shaheen, A. Abbas, Y. Zaman, M.U. Rasheed, A. Karim, M. Mustaqeem, M. F. ur Rehman, M.M. Alam, A.S. Alahmari, *Carissa macrocarpa* extract based greenly synthesized AuNPs: a sustainable approach for lead ion detection, Azo dye degradation, and antimicrobial applications, Water Air Soil Pollut. 236 (6) (2025), https://doi.org/10.1007/s11270-025-08014-x.
[16] C. Malarkodi, S. Rajeshkumar, M. Vanaja, K. Paulkumar, G. Gnanajobitha, G. Annadurai, Eco-friendly synthesis and characterization of gold nanoparticles using *Klebsiella pneumoniae*, Journal Of Nanostructure in Chemistry 3 (30) (2013) 1–7. http://www.jnanochem.com/content/3/1/30.
[17] M. Paesa, C. Remirez de Ganuza, T. Alejo, C. Yus, S. Irusta, M. Arruebo, V. Sebastian, G. Mendoza, Elucidating the mechanisms of action of antibiotic-like ionic gold and biogenic gold nanoparticles against bacteria, J. Colloid Interface Sci. 633 (2023) 786–799, https://doi.org/10.1016/j.jcis.2022.11.138.
[18] A. Thirumurugan, S. Ramachandran, N.A. Tomy, G.J. Jiflin, G. Rajagomathi, Biological synthesis of gold nanoparticles by *Bacillus subtilis* and evaluation of increased antimicrobial activity against clinical isolates, Kor. J. Chem. Eng. 29 (12) (2012) 1761–1765, https://doi.org/10.1007/s11814-012-0055-7.
[19] M. Mpeta, J.T. Tendenedzai, S.M. Tichapondwa, E.M.N. Chirwa, Performance evaluation of gold (III) bio-reduction by bacterial strains and a consortium isolated from gold mine effluent, Minerals Engineering Journal 235 (June 2025) (2025), https://doi.org/10.1016/j.mineng.2025.109797.
[20] P. Pourali, O. Benada, M. Pátek, E. Neuhöoferová, V. Dzmitruk, V. Benson, Response of biological gold nanoparticles to different pH values: is it possible to

prepare both negatively and positively charged nanoparticles? Applied Sciences (Switzerland) 11 (23) (2021) https://doi.org/10.3390/app112311559.
[21] H. Duman, E. Akda, Gold nanoparticles : Multifunctional properties , synthesis , and future prospects, Nanomaterials 14 (22) (2024) 1805, https://doi.org/10.3390/nano14221805.
[22] J.T. Tendenedzai, E.M.N. Chirwa, H.G. Brink, Performance evaluation of selenite (SeO_3^{2-}) reduction by *enterococcus spp*, Catalysts 11 (9) (2021), https://doi.org/10.3390/catal11091024.
[23] S.K. Khore, S.R. Kadam, S.D. Naik, B.B. Kale, R.S. Sonawane, Solar light active plasmonic Au@TiO_2 nanocomposite with superior photocatalytic performance for H_2 production and pollutant degradation, New J. Chem. 42 (13) (2018) 10958–10968, https://doi.org/10.1039/c8nj01410h.
[24] R.J. Neama, F.K.M. Alosfur, K.J. Tahir, N.J. Ridha, L.M. Ahmed, Preparation of Au-Doped two-phase TiO_2 nanoparticles by one-step method as photocatalytic applications, Indones. J. Chem. 24 (4) (2024) 1117–1134, https://doi.org/10.22146/ijc.92687.
[25] A. Karnwal, R.S. Kumar Sachan, I. Devgon, J. Devgon, G. Pant, M. Panchpuri, A. Ahmad, M.B. Alshammari, K. Hossain, G. Kumar, Gold nanoparticles in nanobiotechnology: from synthesis to biosensing applications, ACS Omega 9 (28) (2024) 29966–29982, https://doi.org/10.1021/acsomega.3c10352.
[26] M. Shah, V. Badwaik, Y. Kherde, H.K. Waghwani, T. Modi, Z.P. Aguilar, H. Rodgers, W. Hamilton, T. Marutharaj, C. Webb, M.B. Lawrenz, R. Dakshinamurthy, Gold nanoparticles: various methods of synthesis and antibacterial applications, Frontiers in Bioscience - Landmark 19 (8) (2014) 1320–1344, https://doi.org/10.2741/4284.
[27] S.A. Khan, A. Ahmad, Enzyme mediated synthesis of water-dispersible, naturally protein capped, monodispersed gold nanoparticles, their characterization and mechanistic aspects, RSC Adv. 4 (15) (2014) 7729–7734, https://doi.org/10.1039/c3ra43888k.
[28] T.A. Munyayi, B.C. Vorster, D.W. Mulder, The effect of capping agents on gold nanostar stability, functionalization, and colorimetric biosensing capability, Nanomaterials 12 (14) (2022), https://doi.org/10.3390/nano12142470.
[29] I. Yazgan, A. Gümüş, K. Gökkuş, M.A. Demir, S. Evecen, H.A. Sönmez, R.M. Miller, F. Bakar, A. Oral, S. Popov, M.S. Toprak, On the effect of modified carbohydrates on the size and shape of gold and silver nanostructures, Nanomaterials 10 (7) (2020) 1–17, https://doi.org/10.3390/nano10071417.
[30] S.S. Low, M. Yew, C.N. Lim, W.S. Chai, L.E. Low, S. Manickam, B.T. Tey, P.L. Show, Sonoproduction of nano- biomaterials – a critical review, Ultrason. Sonochem. 82 (November 2021) (2022) 105887, https://doi.org/10.1016/j.ultsonch.2021.105887.
[31] P. Mukherjee, A.K. Nandi, Growth of Different Shape Au Nanoparticles through an Interfacial Redox Process Using a Conducting, Polymer 26 (21) (2010) 2785–2790, https://doi.org/10.1021/la902833q.
[32] A.R. Binupriya, M. Sathishkumar, K. Vijayaraghavan, S.I. Yun, Bioreduction of trivalent aurum to nano-crystalline gold particles by active and inactive cells and cell-free extract of *Aspergillus oryzae var. viridis*, J. Hazard Mater. 177 (1–3) (2010) 539–545, https://doi.org/10.1016/j.jhazmat.2009.12.066.
[33] E. Tomaszewska, K. Soliwoda, K. Kadziola, B. Tkacz-Szczesna, G. Celichowski, M. Cichomski, W. Szmaja, J. Grobelny, Detection limits of DLS and UV-Vis spectroscopy in characterization of polydisperse nanoparticles colloids, J. Nanomater. 2013 (2013), https://doi.org/10.1155/2013/313081.
[34] X. Luo, X. Xie, Y. Meng, T. Sun, J. Ding, W. Zhou, Ligands dissociation induced gold nanoparticles aggregation for colorimetric Al^{3+} detection, Anal. Chim. Acta 1087 (December) (2019) 76–85, https://doi.org/10.1016/j.aca.2019.08.045.
[35] C.H. Luo, V. Shanmugam, C.S. Yeh, Nanoparticle biosynthesis using unicellular and subcellular supports, NPG Asia Mater. 7 (8) (2015), https://doi.org/10.1038/am.2015.90.
[36] S. Pasieczna-Patkowska, M. Cichy, J. Flieger, Application of fourier transform infrared (FTIR) spectroscopy in characterization of green synthesized nanoparticles, Molecules 30 (3) (2025) 1–36, https://doi.org/10.3390/molecules30030684.
[37] K. Lim, F.C. Macazo, C. Scholes, H. Chen, K. Sumampong, S.D. Minteer, Elucidating the mechanism behind the Bio- nanomanufacturing of gold nanoparticles using *Bacillus subtilis*, ACS Appl. Bio Mater. 3 (6) (2020) 3859–3867, https://doi.org/10.1021/acsabm.0c00420.
[38] X. Bai, Y. Wang, Z. Song, Y. Feng, Y. Chen, D. Zhang, L. Feng, The basic properties of gold nanoparticles and their applications in tumor diagnosis and treatment, Int. J. Mol. Sci. 21 (7) (2020), https://doi.org/10.3390/ijms21072480.
[39] C.G. Yuan, C. Huo, B. Gui, W.P. Cao, Green synthesis of gold nanoparticles using *Citrus maxima* peel extract and their catalytic/antibacterial activities, IET Nanobiotechnol. 11 (5) (2017) 523–530, https://doi.org/10.1049/iet-nbt.2016.0183.
[40] S.S. Sana, R. Mukherjee, T.H. Oh, A. Tufail, G. Das, S.C. Kim, A. Dubey, Developing biocompatible chitosan-stabilized gold nanoparticles with anticancer and antimicrobial properties: a computational and experimental approach, ACS Appl. Bio Mater. 8 (9) (2025) 8352–8378, https://doi.org/10.1021/acsabm.5c01281.
[41] J. Li, Q. Li, X. Ma, B. Tian, T. Li, J. Yu, S. Dai, Y. Weng, Y. Hua, Biosynthesis of gold nanoparticles by the extreme bacterium *Deinococcus radiodurans* and an evaluation of their antibacterial properties, Int. J. Nanomed. 11 (2016) 5931–5944, https://doi.org/10.2147/IJN.S119618.
[42] D. Lahiri, M. Nag, H.I. Sheikh, T. Sarkar, H.A. Edinur, S. Pati, R.R. Ray, Microbiologically- synthesized nanoparticles and their role in silencing the biofilm signaling Cascade, Front. Microbiol. 12 (February) (2021), https://doi.org/10.3389/fmicb.2021.636588.
[43] M.A. Waideman, V.P. Teixeira, E.H. Uemura, T.M. Stamford, D.A. Guiguet Leal, L. Stangarlin-Fiori, S.M. Rodrigues Ferreira, C.A. Taconeli, M.R. Beux, *Enterococci* used as complementary indicator of fecal contamination to assess water quality from public schools in the city of curitiba, Paraná, Brazil, Braz. J. Food Technol. 23 (2020) 1.
[44] M. Chowdhury, I. Laiz, I. de la Calle, Sentinel-2 enabled *E. coli* and *Enterococcus Faecal* bacteria surveillance in coastal-recreational waters, Sci. Rep. 15 (1) (2025) 1–14, https://doi.org/10.1038/s41598-025-11233-1.
[45] D. Chang, L. Sharma, C.S. Dela Cruz, D. Zhang, Clinical epidemiology, risk factors, and control strategies of *Klebsiella pneumoniae* infection, Front. Microbiol. 12 (December) (2021) 1–9, https://doi.org/10.3389/fmicb.2021.750662.
[46] R. Itani, H.M.J. Khojah, R. Kibrit, H. Raychouni, P. Shuhaiber, C. Dib, M. Hassan, T. L. Mukattash, A. El-Lakany, Risk factors associated with multidrug-resistant *Klebsiella pneumoniae* infections, BMC Public Health 24 (1) (2024), https://doi.org/10.1186/s12889-024-20474-0.
[47] R.M. Martin, M.A. Bachman, Colonization, infection, and the accessory genome of Klebsiella pneumoniae, Front. Cell. Infect. Microbiol. 8 (JAN) (2018) 1–15, https://doi.org/10.3389/fcimb.2018.00004.
[48] A. Ahmed, A.K. Khan, A. Anwar, S.A. Ali, M.R. Shah, Biofilm inhibitory effect of chlorhexidine conjugated gold nanoparticles against *Klebsiella pneumoniae*, Microb. Pathog. 98 (September) (2016) 50–56, https://doi.org/10.1016/j.micpath.2016.06.016.
[49] M. Khosravi, A. Mirzaie, A.B. Kashtali, H. Noorbazargan, Antibacterial, anti-efflux, anti-biofilm, anti-slime (exopolysaccharide) production and urease inhibitory efficacies of novel synthesized gold nanoparticles coated *Anthemis atropatana* extract against multidrug- resistant *Klebsiella pneumoniae* strains, Arch. Microbiol. 202 (8) (2020) 2105–2115, https://doi.org/10.1007/s00203-020-01930-y.
[50] X. Li, H. Xu, Z.S. Chen, G. Chen, Biosynthesis of nanoparticles by microorganisms and their applications, J. Nanomater. 2011 (2011), https://doi.org/10.1155/2011/270974.
[51] Y. Pan, A. Leifert, D. Ruau, S. Neuss, J. Bornemann, G. Schmid, W. Brandau, U. Simon, W. Jahnen-Dechent, Gold nanoparticles of diameter 1.4 nm trigger necrosis by oxidative stress and mitochondrial damage, Small 5 (18) (2009) 2067–2076, https://doi.org/10.1002/smll.200900466.
[52] A.N. Dosumu, S. Claire, L.S. Watson, P.M. Girio, S.A.M. Osborne, Z. Pikramenou, N. J. Hodges, Quantification by luminescence tracking of red emissive gold nanoparticles in cells, JACS Au 1 (2) (2021) 174–186, https://doi.org/10.1021/jacsau.0c00033.
[53] S. Shikha, V. Kumar, A. Jain, D. Dutta, M.S. Bhattacharyya, Unraveling the mechanistic insights of sophorolipid-capped gold nanoparticle-induced cell death in *Vibrio cholerae*, Microbiol. Spectr. 11 (6) (2023) 1–19, https://doi.org/10.1128/spectrum.00175-23.
[54] A.T. Le, S.Y. Pung, S.L. Chiam, N.A.H.B.N. Josoh, T.Y. Koay, J.S. Lee, N.B. Mustar, Photocatalytic performance of TiO_2 particles in degradation of various organic dyes under visible and UV light irradiation, AIP Conf. Proc. 2267 (February 1972) (2020), https://doi.org/10.1063/5.0016025.
[55] E. Han, K. Vijayarangamuthu, J. sang Youn, Y.K. Park, S.C. Jung, K.J. Jeon, Degussa P25 TiO_2 modified with H_2O_2 under microwave treatment to enhance photocatalytic properties, Catal. Today 303 (August 2017) (2018) 305–312, https://doi.org/10.1016/j.cattod.2017.08.057.
[56] Y. Shiraishi, N. Yasumoto, J. Imai, H. Sakamoto, Electronic Supplementary Information (ESI) Quantum Tunneling Injection of Hot Electrons in Au/TiO_2 Plasmonic Photocatalysts, 2017, pp. 1–17.
[57] Y. Shiraishi, N. Yasumoto, J. Imai, H. Sakamoto, S. Tanaka, S. Ichikawa, B. Ohtani, T. Hirai, Quantum tunneling injection of hot electrons in Au/TiO_2 plasmonic photocatalysts, Nanoscale 9 (24) (2017) 8349–8361, https://doi.org/10.1039/c7nr02310c.
[58] Y. Liu, L. Chen, J. Hu, J. Li, R. Richards, TiO_2 nanoflakes modified with gold nanoparticles as photocatalysts with high activity and durability under near UV irradiation, J. Phys. Chem. C 114 (3) (2010) 1641–1645, https://doi.org/10.1021/jp910500c.
[59] T.H.M. Wint, M.F. Smith, N. Chanlek, F. Chen, T.Z. Oo, P. Songsiriritthigul, Physical origin of diminishing photocatalytic efficiency for recycled TiO_2 nanotubes and ag-loaded TiO_2 nanotubes in organic aqueous solution, Catalysts 10 (7) (2020) 1–13, https://doi.org/10.3390/catal10070737.
[60] B.B. Tripathy, M. Behera, H. Rath, P. Mallick, N.C. Mishra, Evolution of microstructure and optical properties of TiO_2/Au nanocomposite, Indian J. Pure Appl. Phys. 57 (2) (2019) 95–100.
[61] K.M. Rahulan, S. Ganesan, P. Aruna, Synthesis and optical limiting studies of Au-doped TiO_2 nanoparticles, Adv. Nat. Sci. Nanosci. Nanotechnol. 2 (2) (2011), https://doi.org/10.1088/2043-6262/2/2/025012.
[62] X. Guo, H. Wang, L. Wang, D. Zeng, Q. Xiang, B. Chai, Triple-mode Bi_2WO_6/Pg-C_3N_4 @rGO core-shell synergistic effect with enhanced light-induced photocatalytic activity, Bull. Kor. Chem. Soc. 40 (3) (2019) 254–261, https://doi.org/10.1002/bkcs.11675.
[63] D. Yang, Y. Xia, T. Xiao, Z. Xu, Y. Lei, Y. Jiao, X. Zhu, W. Feng, Constructing Ag–TiO_2-g-C_3N_4 S-scheme heterojunctions for photocatalytic degradation of malachite green, Opt. Mater. 159 (February) (2025) 1–9, https://doi.org/10.1016/j.optmat.2025.116652.
[64] A. Ejaz, Z. Mamtaz, I. Yasmin, M. Shaban, A.B. Siddique, M.I. Irfan, A. Ali, S. Muhammad, M.Y. Sameeh, A. Abbas, *Cyperus scariosus* extract based greenly synthesized gold nanoparticles as colorimetric nanoprobe for Ni^{2+} detection and as antibacterial and photocatalytic agent, J. Mol. Liq. 393 (2024) 1–11, https://doi.org/10.1016/j.molliq.2023.123622.
[65] A.W. Khan, N.S. Lali, F.Y. Sabei, M.I. Irfan, M. Naeem-ul-Hassan, M. Sher, A. Y. Safhi, A. Alsalhi, A.H. Albariqi, F. Kamli, H.M.A. Amin, A. Abbas, Sunlight-assisted green synthesis of gold nanocubes using horsetail leaf extract: a highly selective colorimetric sensor for Pb^{2+}, photocatalytic and antimicrobial agent,

J. Environ. Chem. Eng. 12 (3) (2024) 1–12, https://doi.org/10.1016/j.jece.2024.112576.

[66] H. Ahmad, A.B. Siddique, S. Zaheer, R. Sattar, A. Abbas, M. Amin, R. Al-Salahi, H. A. Abuelizz, M.Z. Saleem, Energy bandgap tuning of Sr-doped ZnO nanoparticles for photodegradation of azo dyes and antibacterial applications, Journal of Water Process Engineering 74 (2025) 1–11, https://doi.org/10.1016/j.jwpe.2025.107855.

[67] G. Žerjav, M. Roškarič, J. Zavašnik, J. Kovač, A. Pintar, Effect of Au loading on Schottky barrier height in TiO_2 + Au plasmonic photocatalysts, Appl. Surf. Sci. 579 (March) (2022) 1–10, https://doi.org/10.1016/j.apsusc.2021.152196.

[68] S. Loukopoulos, E. Sakellis, P. Tsipas, S. Gardelis, V. Psycharis, M.G. Kostakis, N. S. Thomaidis, V. Likodimos, Visible-light-responsive Ag (Au)/MoS_2-TiO_2 inverse opals: synergistic plasmonic, photonic, and charge transfer effects for photoelectrocatalytic water remediation, Nanomaterials 15 (14) (2025) 1–21, https://doi.org/10.3390/nano15141076.

[69] L.G. Devi, R. Kavitha, A review on plasmonic metal-TiO_2 composite for generation, trapping, storing and dynamic vectorial transfer of photogenerated electrons across the schottky junction in a photocatalytic system, Appl. Surf. Sci. 360 (January) (2016) 601–622, https://doi.org/10.1016/j.apsusc.2015.11.016.